atoms

MDPI

Article

EUV Beam-Foil Spectra of Titanium, Iron, Nickel, and Copper

Elmar Träbert [1,2]

[1] Fakultät für Physik und Astronomie, Ruhr-Universität Bochum, AIRUB, 44780 Bochum, Germany; traebert@astro.rub.de; Tel.: +49-2343223451; Fax: +49-2343214169
[2] Lawrence Livermore National Laboratory, Physics Division, Livermore, CA 94550-9234, USA

Abstract: Beam–foil spectroscopy offers the efficient excitation of the spectra of a single element as well as time-resolved observation. Extreme-ultraviolet (EUV) beam–foil survey and detail spectra of Ti, Fe, Ni, and Cu are presented, as well as survey spectra of Fe and Ni obtained at an electron beam ion trap. Various details are discussed in the context of line intensity ratios, yrast transitions, prompt and delayed spectra, and intercombination transitions.

Keywords: atomic physics; EUV spectra; beam–foil spectroscopy

check for updates

Citation: Träbert, E. EUV Beam-Foil Spectra of Titanium, Iron, Nickel, and Copper. *Atoms* **2021**, *9*, 45. https://doi.org/10.3390/atoms9030045

Academic Editor: Jean-Christophe Pain

Received: 16 June 2021
Accepted: 6 July 2021
Published: 13 July 2021

1. Introduction

Bengt Edlén demonstrated by laboratory experiments in the 1940s [1] that the long-time mysterious solar corona lines (in the visible spectrum) originated from electric-dipole forbidden transitions in the ground configurations of highly charged ions of Ca, Fe, and Ni, a hypothesis Grotrian [2] had formulated on the basis of some of Edlén's earlier measurements of X-ray transitions. When in the 1960s and 1970s sounding rockets and satellites heaved spectrometers beyond Earth's atmosphere and thus opened the new field of direct X-ray and EUV observations of highly charged ions in the solar corona, researchers marveled at the rich EUV and X-ray spectra, especially of Fe. Brian Fawcett, Alan Gabriel, Carole Jordan, and their colleagues recognized that a study of both terrestrial and astrophysical light sources would be mutually beneficial for the investigation of the spectra of iron group elements [3–5]. This insight gave a new common perspective to a multitude of spectroscopy laboratories around the world (among other countries, in Belgium, Canada, France, Japan, the Netherlands, the Soviet Union, Spain, Sweden, the UK, and the USA). Soon after, new laboratory light sources such as low-pressure plasma discharges for fusion research, laser-produced plasmas, and foil-excited ion beams began to expand the spectroscopy toolbox that, for highly charged ions, had hitherto largely depended on a variety of spark discharges.

Kelly and Palumbo produced early wavelength compilations of UV, EUV, and X-ray experimental data from many such studies [6,7]). Fawcett approached the problem systematically by combining experimental data with semi-empirically scaled Hartree–Fock computations, providing some of the earliest wide-range tabulations on levels, wavelengths, and transition rates of multiply charged ions [8]. The results of this computational technique are not very precise on their own, but, by an adjustment of Slater parameters, the computations can practically be fitted to the observational data and thus the consistency of the data can be checked at a high quality level [9]. The US National Bureau of Standards (NBS, now NIST) began systematic tabulations (with term analysis) in the 1940s, in addition to in-house spectroscopic work of high quality [10]. Eventually, many of their data holdings have become available as the NIST ASD online database [11]. Shirai, Mori, and colleagues in Japan have separately compiled data on the iron group elements. One of their later publications may serve as a gateway to their many publications [12]. Another database of widespread interest is the result of the CHIANTI project [13–17]. This work addresses primarily astrophysicists and their needs; the objectives, achievements, and perspectives of the CHIANTI project have recently been reviewed by the project members [18]. In the CHIANTI project, Del Zanna and colleagues have built on Fawcett's photographic plates and combined them with the newer observations by sounding rockets (see the SERTS and EUNIS programs [19,20]) and satellites, especially the EIS spectrograph on the *Hinode* spacecraft [21], to derive critically compiled data on many ions that contribute to the spectra of the solar corona, in particular of Fe (see below). Their computed EUV spectra (modeled for various electron densities and temperatures as occur in the solar corona) help with the analysis and understanding of stellar spectra.

Instruments such as *Hinode*/EIS are among the best available for their respective ranges of operation, and yet the interpretation of the complex solar spectra remains a challenge. The EUV part of the electromagnetic spectrum may be dominated by "merely" a few thousand lines, but the spectral resolving power of typical spectrographs is far from sufficient to resolve all significant blends. In a trade-off between spectral discrimination and sufficient signal, sometimes a wider bandwidth is chosen for the benefit of a high signal-to-noise ratio, as well as for a high signal cadence that yields access to time-varying phenomena. The interpretation of a signal that is known to originate from several ion species combined then depends on a comprehensive modeling effort. An example is the AIA experiment on board the $SolarDynamicsObservatory(SDO)$ [22] that determines coronal temperatures from a combination of observations of EUV lines, mostly of Fe. However, spectral modeling depends on data, and, in the last two decades, it has become apparent that spectral models and their data bases do not necessarily agree in the position of spectral lines with observations by space observatories such as *Chandra*, $XMM - Newton$ or *Hinode*, or with high-resolution laboratory data from electron beam ion traps (EBIT) [23]. A laboratory effort at the Livermore EBIT therefore attempted to support the *SDO* project by recording element-specific high-resolution EUV spectra of the wavelength bands of the low-resolution *SDO* detectors [24–29]. The laboratory spectra were intended to clarify the blending situation with lines of other elements, and, in addition, they revealed a multitude of mostly weak unidentified lines of identifiable elements as well. This corresponds to a general experience with astrophysical EUV spectra that contain many unidentified weak lines of unidentified elemental origin.

The excitation conditions in an EBIT are rather close in (very low) electron density to those in a stellar corona. In contrast, the excitation conditions in a foil-excited ion beam traversing a carbon foil (with its solid-state electron density) are very different from the astrophysical environment. However, the latter technique provides isotopically pure spectra and thus can contribute to the analysis of coronal EUV spectra even if the spectral resolution is typically poorer than that of the spacecraft spectrographs. This contribution of data are one of the goals of the present study and its companions (on K and C [30], and on Sc, V, Cr, Mn, Co, Zn [31]) which together span the range of elements from $Z = 19$ to 30.

The interpretation of astrophysical spectra leans heavily on theoretical support. On the one hand, atomic structure theory is highly developed and provides accurate results on few-electron ions of all elements. On the other hand, with more than two electrons in the valence shell, the complexity of the problem is usually too high for computations of spectroscopic accuracy. It may be disputed whether this is a problem of theory (quantum mechanics and QED seem firmly established) or rather of the computational implementation of a complex many-body problem. Moreover, substantial inaccuracies plague the computation of transition rates in many-electron systems. However, the best computations have helped with finding a fair number of (rare) misidentifications in earlier spectroscopic analyses, and the results are often highly useful in guiding identification attempts through new territory. Different approximations and computational approaches yield somewhat different results, resulting in a certain scatter among computational findings. Examples of recent computations on isoelectronic sequences that include ions of present interest (isoelectronic sequences F, Ne, Mg, Si, S) are [32–43] and references cited therein. Among the ab initio approaches with the most accurate results are Multireference Møller–Plesset computations of the Ishikawa group, MCDHF computations employing versions of the

GRASP code, and RMBPT computations (for unfolding the akronyms and details of the approaches, see a recent review by Jönsson et al. [44]). Examples below demonstrate a few cases in which high accuracy has been achieved, as well as some others.

The present study does not comprise new computations, nor many results of experiments distilled to numbers, as have been presented elsewhere. Various studies that did aim at such numbers (wavelengths, level energies, level lifetimes, etc.) are being cited below. Those dedicated studies usually concentrate on certain details and features of spectra, and, for a lack of space in printed journals, they do not show survey spectra or sections of spectra outside their particular range of interest. Later researchers therefore would have to perform their own experiments to gain access to possibly already measured, but unpublished data. This is not always practical or even possible. Moreover, some of the earlier work has presented spectra in a graphical form, but the wide-spread later process of digitisation of such publications involved scanning the earlier journal pages, often at suboptimal quality, and many such reproductions are barely readable. The emphasis of the present study is on a presentation of data plotted digitally to begin with (from the original data files) and thus being preserved for inspection. The spectra are selected for maximum wavelength coverage and accompanied by comments to explain the purpose and notable particulars for the benefit of readers who search for details that have not been explained before. The vast majority of the strong lines in the spectra is known, and their wavelengths are well established and available in databases. However, some of the data compilations have historical gaps that can be checked by referring to raw data. Moreover, measured spectra often comprise a large numbers of weak lines that have not yet been classified. For the beam–foil data presented below (many of which served specific goals in other studies), at least the elemental identity is certain, and the charge state can be approximated from the recording conditions. The graphical displays are meant to be immediately useable.

2. Beam–Foil Spectra

More than half a century after Fawcett and Gabriel's pioneering studies [3–5], it may be appropriate to help fill some of the gaps in the knowledge, based on beam–foil spectra that I have retrieved from storage. (Numerous data sets have been lost due to the mishaps of data storage media and computer system changes over several decades.) The recordings were made at the Bochum tandem accelerator laboratory about 30 years ago starting out with observations of electric dipole (E1) transitions, decay curves of regular and displaced terms, and various isoelectronic studies of specific configurations (for examples of such work on elements of present emphasis, see [45–54]). From this work, a quest evolved for finding spin-changing intercombination lines in iron group ions with an open $n = 3$ valence shell, and for measuring their transition rates (see, for example, [55–60]). In order to gain a perspective on the spectra under study, survey spectra were recorded for most elements before turning to detail spectra. It is these surveys that I want to preserve for public access, so that other researchers can use them for their orientation. A number of detail spectra are to be shown as well, supplemented by explanations of why I consider them noteworthy.

Of course, the work at Bochum was not singular in Europe, where accelerator-based atomic physics was pursued in many laboratories (to name a few: Aarhus, Berlin, Bielefeld, Caen, Copenhagen, Darmstadt, Kaiserslautern, Liège, Lund, Lyon, Munich, Oxford, Stockholm, and Uppsala, plus numerous US American and Canadian laboratories). It just happened that, at Bochum, the accelerator type (selected by researchers from three universities for certain nuclear physics experiments) and ion source capabilities turned out to be eminently suitable for atomic physics studies of many elements in the first third of the table of the elements. Because of the versatility of the facility, those elements could also be studied that found less interest or encountered too much experimental difficulty elsewhere.

The beam–foil measurement technique has been recalled in various reviews (see [61,62] and references therein) and in two recent companion papers [30,31]. The spectra shown in this study have been obtained at the Bochum Dynamitron tandem accelerator laboratory (DTL), where a 4 MV tandem accelerator equipped with a sputter ion source [63,64] provided ion beams of more than 40 elements, with an energy from a few MeV up to about 30 MeV, and with beam currents (particle current) in the range from 0.1 μA to several μA of most iron group elements. The ion beam with its typical velocity of about 1 cm/ns (3% of the speed of light) was passed through a thin carbon foil of areal density 10 μg/cm^2 in which it lost a small fraction of its energy. The ions lose and capture electrons in the interaction with the electrons in the foil (at solid-state density) and emerge with a distribution of charge states (see [65–67]).

A grazing-incidence spectrometer (McPherson Model 247) equipped with an $R = 2.2$ m grating of groove density 600 ℓ/mm dispersed the EUV radiation emitted by the excited ions. A channeltron served as the detector behind the exit slit of the scanning instrument. For many purposes, it would have been advantageous to use a position-sensitive multi-channel detector as has been exploited elsewhere (for an early example, see [68,69]). However, this was not to happen at Bochum.

For the EUV monochromator drive, the original synchronous motor was soon replaced by a stepper motor. Data acquisition initially used a multichannel scaler, and all channel timing and signal normalisation (to accumulated ion beam charge on a Faraday cup) operated on a single choice of preset settings. Over the years, this measurement control system graduated to a Commodore PET personal computer (first demonstrated in this laboratory in the group of H. H. Bukow) and then to an Apple IIe. The latter enabled varied and optimized settings of charge normalization and thus of data accumulation time as well as tailored stepper motor increments during a given recording of a spectrum or a decay curve. This option was used to optimize the beam time spent on more or less significant sections of a recording. For example, it became possible to cover several reference lines in a spectrum with good counting statistics while stepping quickly through less interesting sections, all the time relying on a single initial spectrometer setting and sometimes a single wavelength reference. In a decay curve, data points could be chosen with a dense pattern where—close to the foil—short-lived components mattered, and with wider spacings for the drawn-out tail dominated by slow components. Of course, it happened several times that in hindsight the experimenters would have liked to collect statistically better data also in the low-preset sections, as is demonstrated by examples below. Not all measurements went according to plan, and not all plans worked out as intended. Some of the experiences and mishaps are explained along the way as a means to help judge the experimental technique, its offerings, and its limitations.

For example, following good experiences with such a device at Oxford [70], a Heidenhain Moiré fringe length gauge with a 60 mm travel and reading positions to ±1 μm was attached to the grazing incidence monochromator. This device quickly revealed a small, but quite notable, periodic error on the lead screw of the spectrometer and thus enabled much more accurate wavelength difference measurements. However, when employed in survey scans, the length gauge had to be shifted and reset about every 50 mm to follow the exit slit head. In the repositioning, the home-built gauge mount repeatedly suffered slight changes of alignment, which became notable only after the offline calibration of the measured spectra. A length gauge covering the full range of travel of the exit slit head (about half a meter) was not available at the time and would have required substantial changes in the spectrometer design. However, such a device (possibly incorporating an absolute reference marker) would have indicated the occasional slips between the drive system and the mechanical position read-out, as well as a variety of backlash problems that evolved (and gradually worsened) over the quarter of a century of spectrometer use.

Besides Fe ($Z = 26$), the other even-numbered elements of the iron group (Ti ($Z = 22$), Cr ($Z = 24$), and Ni ($Z = 28$)) have been studied mostly in terrestrial spectra, although their abundance allows for expecting some prominence also in astrophysical spectra. Of these, Cr has been covered in a recent companion paper [31]. On the other hand, the odd-numbered element Cu ($Z = 29$) is not very abundant in space and thus not prominent in astrophysical spectra. However, Cu has been used for electrical conductors such as antennas in fusion research plasma experiments and thus might contaminate those spectra. Moreover, Cu ions yield a high ion beam current in accelerator experiments, which renders them readily available and useful for comparisons with Ni spectra. In the following, Bochum beam–foil data on the four elements Ti, Fe, Ni, and Cu are shown and explained.

In the range of elements and ion charge states covered in the present investigation, there is a trend that relates to the heavy-ion tandem accelerator employed. This is an electrostatic accelerator, and the ion beam energy can be chosen in a certain range limited by the machine parameters, such as the maximum high voltage at the terminal, which is about 4 MV. Negative ions (singly charged) are produced at about 90 keV and fed to the accelerator at ground potential. The ions are accelerated towards the high voltage terminal in the middle of the tank (at an ion energy of up to 4 MeV) and then passed through a stripper gas. The ions lose electrons and assume a charge state distribution that at an energy of 4 MeV for many elements has a maximum between q = 3+ and 4+. The maximum charge state fraction typically is of order 30%. In the second part of the accelerator, a positively charged ion with $q = 4+$ is further accelerated by the same high voltage U between the terminal and the ground and reach an energy of $E = (q+1)eU$, in our example, 20 MeV. In order to reach 24 MeV, one has to use $q = 5+$, which is available as a significantly lower charge state fraction (and thus lower ion beam current) from the terminal, and so on. Lower voltages are, of course available. The Bochum experiments with Cu beams used ion beam energies of 14 MeV up to 36 MeV. The latter energy requires $q = 8+$, which is produced as a very small fraction (a few percent) of the ion beam after the gas stripper. To produce a beam current producing a sufficient signal in the experiment, the original ion beam current delivered by the ion source has to be correspondingly high. That it succeeded is one of the features that made the Bochum laboratory so exceptionally useful for beam–foil spectroscopy.

2.1. Ti

In the 1950s, Ti was considered an almost exotic material that was difficult to machine. Nowadays, the element is widely used for its many advantageous properties. When in the early 1980s experimenters asked the Bochum accelerator team for a Ti ion beam intended for future guest experiments with Stanley Bashkin [71], one of the inventors of beam–foil spectroscopy, this was still an exploratory process. However, the operators quickly succeeded and turned Ti into one of the strongest ion beams available at this machine, with ion beam particle currents up to about 1 µA on target. Owing to this success, signal rates turned out higher than with many other elements, which in turn permitted observations with higher spectral resolution. The advantage of high spectral resolution is, of course, the reduction of line blends, of which there can be many in such line-rich spectra as the EUV spectra of iron-group elements. Under the right conditions, the resonance lines of ions with a single or two electrons in the valence shell appear prominently. Theory has described such ions with $n = 3$ valence electrons for decades, but the achievement of accuracy has taken time. Na-like ions have been treated very well for about 40 years (see [35]), but ab initio calculations for Mg-like ions have required a couple of decades longer to reach spectroscopic accuracy (for a recent historic view and new treatment, see [36,72]). With a third electron (or more) in the valence shell (Al-like ions), general purpose computations struggle notably. Given the limitations of atomic structure computations at the time, it is no surprise that much later computations of Al-like ions (see [73]) find a fair number of inconsistencies between the various computations and experimental line identifications, including some based on Bochum beam–foil work [74,75]. Nevertheless, beam–foil work on Al-like ions [49] verified assumptions on the variation of line intensity ratios in the $n = 3$ shell for a sequence of elements in the Al I isoelectronic sequence, and the unique properties of the beam–foil light source in combination with advanced computations of Si-like ions [37,38] helped to pin down inconsistencies in earlier term analysis, a problem that popped up with the availability of improved coronal spectra and will be explained in the section on Fe. An atomic structure problem closely related to the two-electron systems is the one-electron—one-vacancy system of singly excited Ne-like ions. For Ti, this is the spectrum Ti XIII, on which Bochum beam–foil work extensively investigated the level structure [76,77] and level lifetimes [78]. At the same time, the Lund group of Litzén and Jupén was involved in studies of laser-produced plasmas of iron-group elements [79], resulting in some parallel analyses (largely agreeing in the level structure and wavelength results with Bochum and Lyon beam–foil work) and several collaborative studies (among others, see [52,53,80–83]). A success of the beam–foil technique is the identification of the Ti XIII $2s^2 2p^5 3p\ ^3S_1$ level decay (to the $2p^5 3s\ ^3P^o_2$ level) by a combination of spectroscopy and lifetime measurements [78]. Interestingly, in the same configuration, the $2s^2 2p^5 3p\ ^1S_0$ level position and decay (two decay channels) are still disputed because candidates for one or both of the two lines are blended in most iron group elements, and the computed level lifetime does not significantly differ from those of many other levels, hence the experiment could not test this parameter for discrimination.

In the course of these studies, it was necessary to record survey spectra that helped to locate the line positions for the intended lifetime measurements. These surveys usually did not advance the accuracy of the literature knowledge on reference lines, but the spectra revealed additional information, only part of which has since been evaluated in detail studies. For example, Jupén has analyzed various yrast transition arrays in F- and Ne-like ions (see, for example, [80]). (Yrast transition is a term phrased by nuclear physicists for transitions between levels of maximum angular momentum ℓ for a given principal quantum number n.) These transitions are particularly prominent in beam–foil spectra because they are fed by chains of other such transitions. Below, there are examples of how such yrast line clusters are identified and enhanced by the observation technique.

Most of the samples of spectra discussed in the following show unpublished data. Where spectra are compared/juxtaposed to each other, they often originate from measurements performed years apart and with different objectives. On purpose, the spectral ranges have not been cut down now to show only details of interest at the time but left as complete as seems reasonable, in order to show details that may possibly become of interest in the future.

Figure 1 shows Ti spectra close to the short-wavelength end of the operating range of the spectrometer. At an ion beam energy of 20 MeV (Figure 1a), the charge state distribution is centered on $q = 11+$, and ion charge states $q = 8+$ to $q = 14+$ are expected to contribute. At an ion beam energy of 10 MeV (Figure 1b), the charge state distribution is centered on $q = 8+$, and ion charge states $q = 6+$ to $q = 11+$ are expected to contribute. Both spectra show n = 3–4 transitions up to the spectrum Ti XII. At the higher ion beam energy (spectrum (a)), the Ti XIII 3d–4f transition array shows with wavelengths near 10 nm. At the lower ion beam energy (spectrum (b)), the charge state Ti^{12+} is not notably produced. However, spectrum (b) shows several weak lines in this wavelength range too, which must originate from lower charge state ions. On the one hand, this example shows the power of charge state discrimination by the choice of the ion beam energy. On the other hand, spectra would have to be recorded at smaller ion beam energy intervals in order to systematically investigate the spectra for contributions of the individual charge state ions. In addition, the prominence of the 3d–4f yrast transitions in all charge states over transitions between levels of lower angular momentum is apparent. This prominence is due to the higher statistical weight (level population) of the 4f levels and the decays being unbranched.

The Ti XIII 3d–4f transition array also features in several other spectra (Figures 2 and 10, discussed below), demonstrating the power of observation in the second diffraction order or of employing a higher groove density diffraction grating. For this spectrum, a grating of 600 L/mm was used.

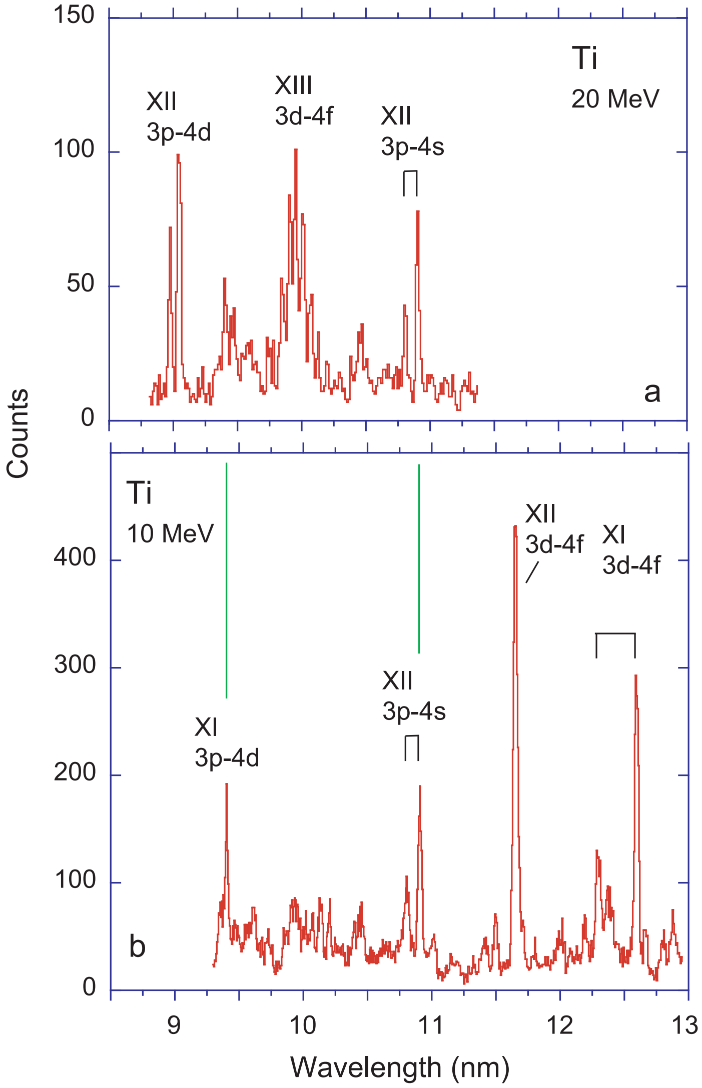

Figure 1. Beam–foil spectra of Ti observed at two ion beam energies (**a**) 20 MeV, (**b**) 10 MeV, line width (FWHM) 0.035 nm. The strongest lines are identified by the spectrum number and transition array. Many of the weak lines remain unidentified so far.

Figure 2 shows a beam–foil spectrum of Ti observed at an ion beam energy of 22 MeV. At this ion beam energy, the charge state distribution is centered on $q = 11+$, and ion charge states $q = 8+$ to $q = 14+$ are expected to contribute. A diffraction grating of high groove density (3600 L/mm) was used, and a line width (FWHM) of 0.006 nm was obtained. Only at such a high resolving power can most of the components of the Ti XIII 3d–4f transition array be resolved. The detail spectrum Figure 2b is based on the same original data as Figure 1 of [83], where the transition array is analyzed. The strongest transitions in the spectrum are identified by the spectrum number. A fair number of weak lines have not yet been identified.

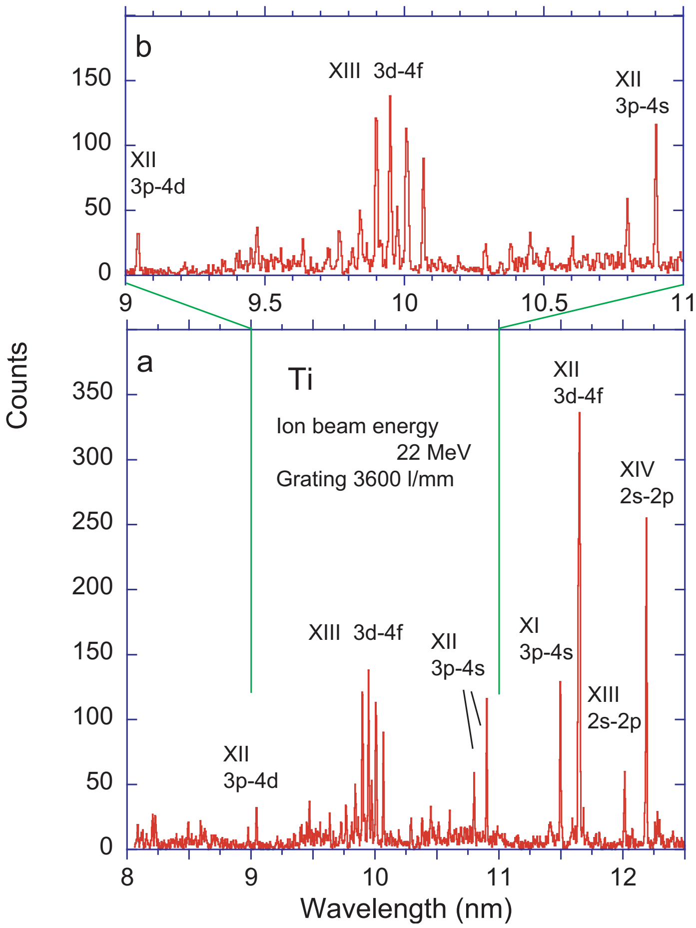

Figure 2. Beam–foil spectrum of Ti observed at an ion beam energy of 22 MeV. Diffraction grating groove density 3600 L/mm, line width (FWHM) of 0.006 nm. (**a**) Survey spectrum; (**b**) expanded detail of the same. The strongest transitions in the spectrum are identified by the spectrum number and transition array. Compare to Figure 1 of [83].

Figure 3 shows beam–foil spectra of Ti recorded at an ion beam energy of 24 MeV. At this ion beam energy, the charge state distribution peaks at $q = 11+$ and $q = 12+$, and ion charge states $q = 9+$ to $q = 15+$ are expected to contribute. Figure 3b includes the second diffraction order image of the spectrum in (a). Hence, several bright lines of (a) also appear in (b) and can serve there as wavelength references in a spectral range that has no convenient first diffraction order Ti lines for this purpose. The two spectra comprise some 20 visually recognizable lines of unknown identity each.

Among the prominent lines of interest are the Ti XII and Ti XIII 4f–5g yrast transition arrays. A prominent line pair is formed by the Ti XIV $2s^22p^5\ ^2P^o_{3/2,1/2}$–$2s2p^6\ ^2S_{1/2}$ lines which have recently found theoretical interest [32,33] and are discussed for elements Ar to Ca in [30]. An interesting point here is the line intensity ratio. An experimental determination with the present equipment is limited in precision by the steep slope of the calibration curve of the spectrometer-cum-grating [84,85]. The present data show almost the same apparent line ratio in first- and second-order observation. However, a calibration curve has been established only for the first-order observation, and it puts the result into rough agreement with prediction.

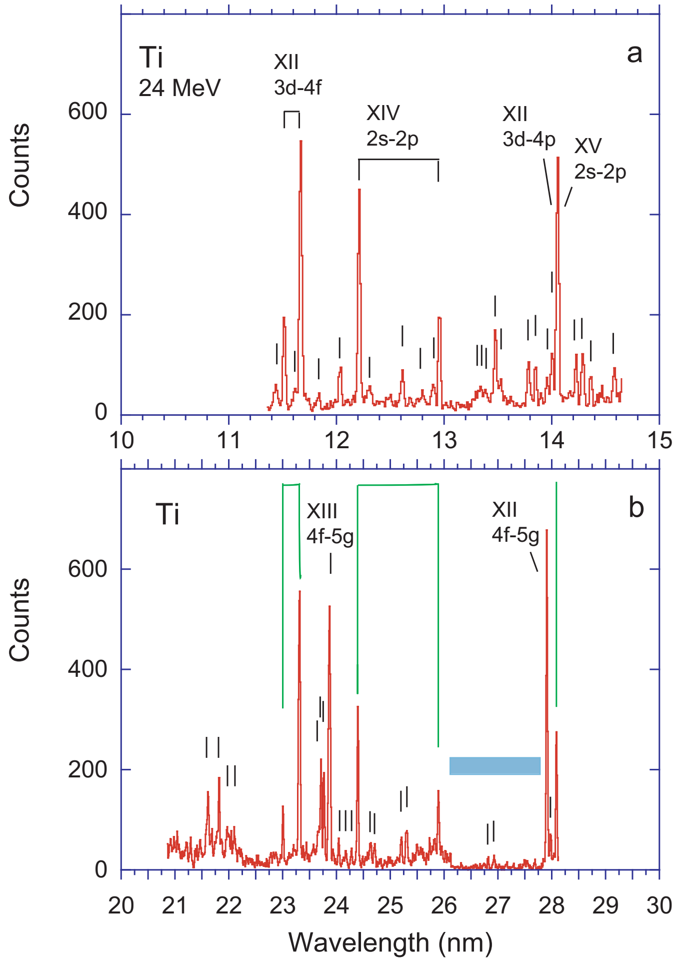

Figure 3. Beam–foil spectra of Ti at an ion beam energy of 24 MeV. Grating 600 L/mm, line width (FWHM) 0.03 nm. The strongest lines are identified by the spectrum number. Unidentified lines are marked by a fiducial. (**a**) Observation of the wavelength range 11.4 nm to 14.6 nm; (**b**) observation of the wavelength range 21 nm to 28 nm, that is, including the second diffraction order image of the spectrum in (**a**). The light blue horizontal bar marks a range of data recording with a reduced ion beam charge preset per channel (see the text).

The Bochum beam–foil spectra of Ti have been investigated variously, most often with a view to the spectra Ti XIII and Ti XIV [76,77,80–83], and several of the publications have included plots of spectral sections. For the benefit of future interest in the raw spectra, Figures 4–8 show consecutive sections of survey spectra recorded at ion beam energies of 10 and 20 MeV, respectively. The charge state distributions expected at these energies are specified in the text for Figure 1. Only a few prominent reference lines are labeled by the spectrum number, and a few vertical green marker lines indicate samples of similar lines in both sets of spectra to make orientation easier when looking for the changes of relative line intensities with variation of the ion beam energy. Since yrast lines are not so prominent in other light sources, these line clusters are labeled. A particularly striking example is the Ti X 4f–5g transition array in the 10 MeV spectrum in Figure 6. Several sections of the 10-MeV spectrum have been recorded with a reduced preset for the ion beam charge normalization so that the scanning monochromator would advance farther in the allotted operation time. This leads to a seemingly wrong intensity ratio of the Ti XII 3s–3p line doublet at 46 nm and 48 nm, where the (expected to be) stronger line appears to be weakened by the shorter recording time per channel and the weaker line strengthened by a line blend with Ti VIII. In the long-wavelength section of the 10-MeV spectrum (Figure 8) (where the spectrometer efficiency runs low [85]), the visually recognized lines have been given markers; most of these lines have not yet been identified from the literature.

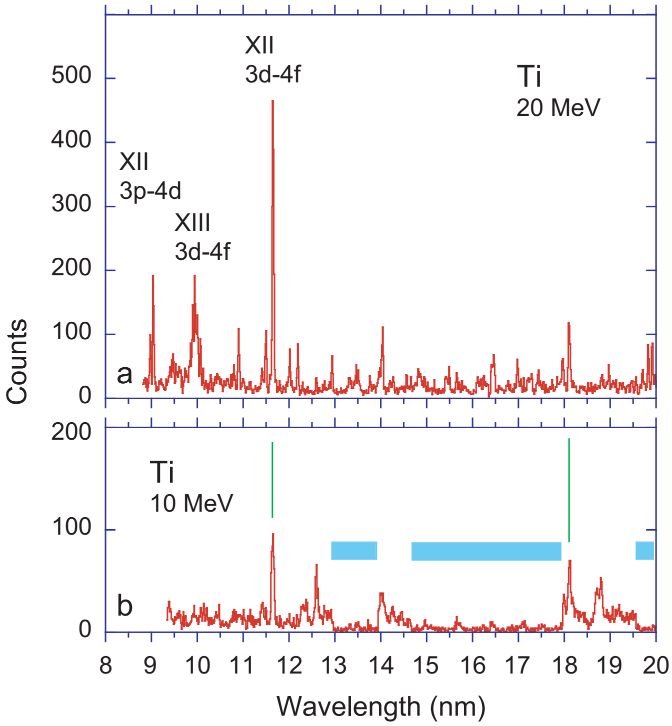

Figure 4. Beam–foil spectra of Ti recorded at ion beam energies of 20 MeV (**a**) and 10 MeV (**b**), respectively. Grating 600 L/mm, line width (FWHM) 0.038 nm in (**a**) and 0.06 nm in (**b**). The strongest lines are identified by the spectrum number. For the charge state distributions, see the legend for Figure 1. The light blue horizontal bars mark ranges of data recording with a reduced ion beam charge preset per channel.

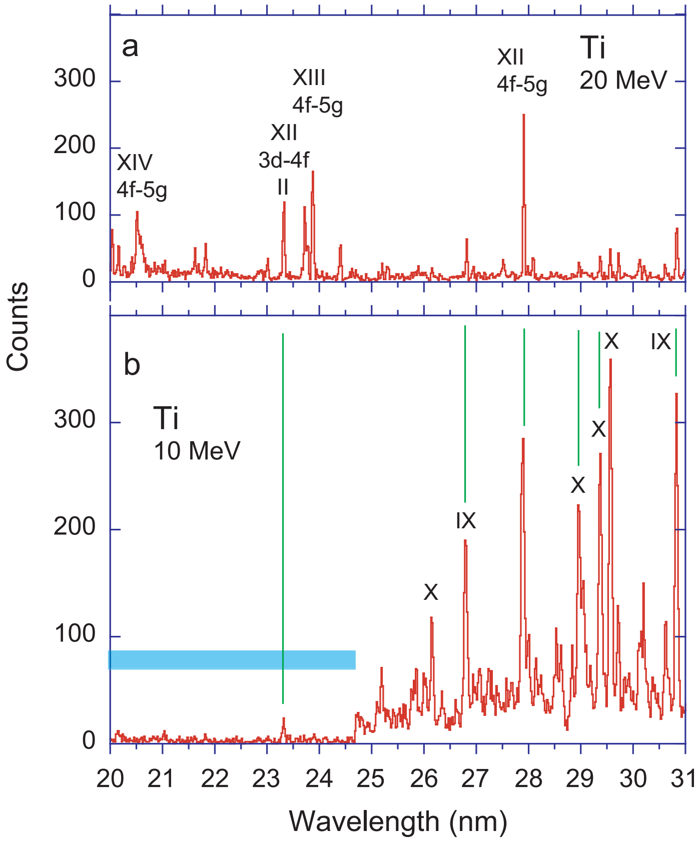

Figure 5. Continuation of the Ti spectra shown in Figure 4. (**a**) ion beam energy 20 MeV, (**b**) ion beam energy 10 MeV.

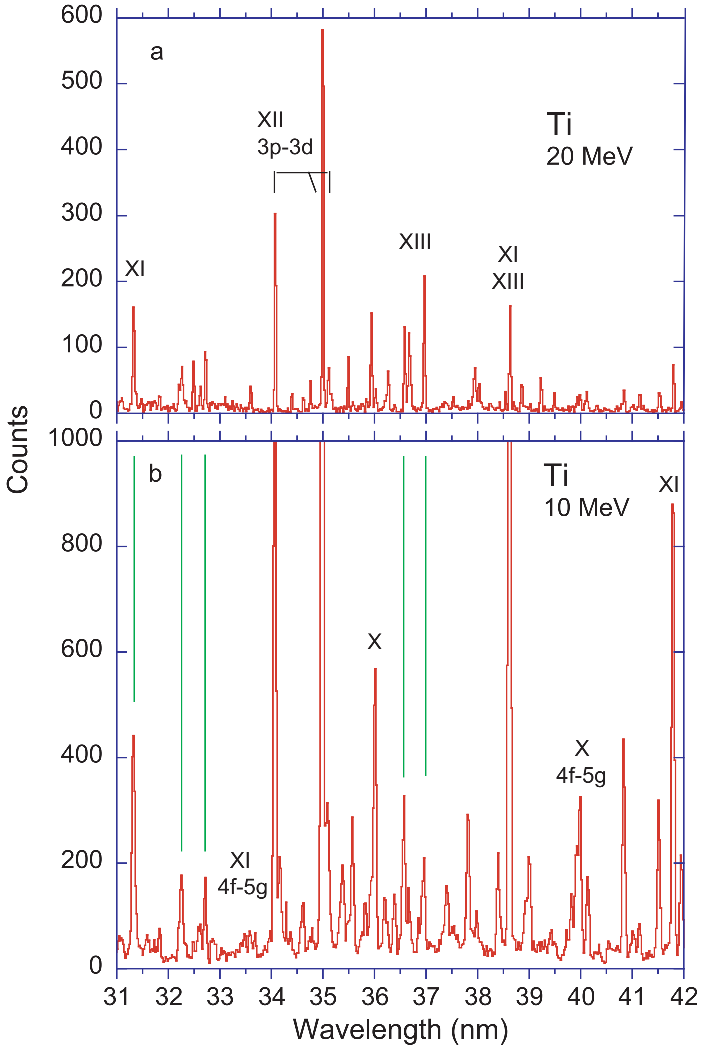

Figure 6. Continuation of the Ti spectra shown in Figures 4 and 5. (**a**) ion beam energy 20 MeV, (**b**) ion beam energy 10 MeV.

Thus far, all spectra concerned prompt electric dipole (E1) decays without spin change. Intercombination transitions (with a change of spin, thus connecting term systems of different multiplicity) have lower transition rates and consequently longer upper level lifetimes, by about two orders of magnitude [86,87] or more. For the E1-allowed decays, a typical upper level lifetime for ions of charge states as discussed so far would be expected in the range of 10 to 200 ps [76,78], whereas the upper level lifetimes of 3s–3p intercombination transitions would be expected in the range of 20 to 1000 ns. The former decays are visible as emission from the ion beam close to the exciter foil (the first few mm), whereas the latter are much weaker per section of the ion beam, but they survive out to distances of many cm from the foil. The EUV detection system at Bochum has a field of view that at the position of the ion beam is just under 1 mm wide. Most of the E1-allowed transitions have a decay length (level lifetime times ion velocity) that is shorter than this distance, and thus, in observations close to the exciter foil, most of the prompt emission happens in this observation window. The decay length of intercombination decays in moderately high charge state ions is on the order of 10 cm and more. This implies that the detection system sees less than 1% of a decay length of such levels, and, due to this geometry effect, the (intrinsically time-resolved) signal of such long-lived decays is roughly two orders of magnitude smaller than that of the resonance transitions.

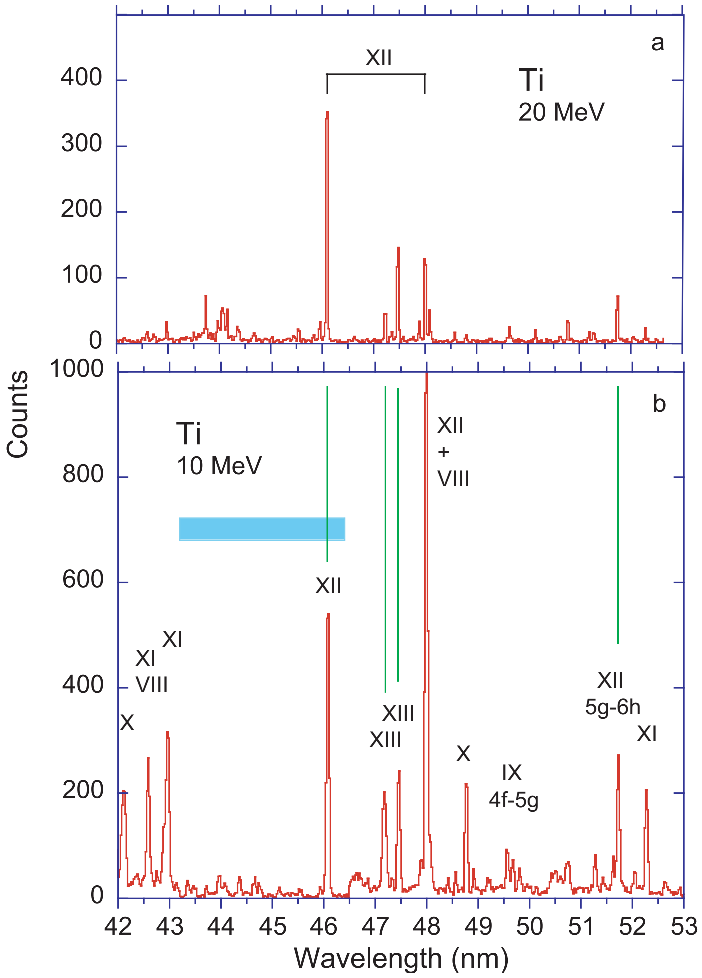

Figure 7. Continuation of the Ti spectra shown in Figures 4–6. (**a**) ion beam energy 20 MeV, (**b**) ion beam energy 10 MeV.

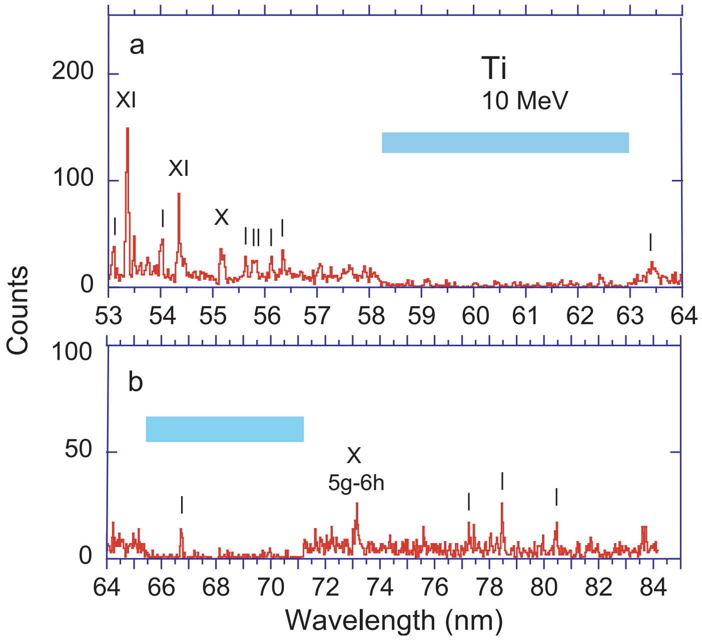

Figure 8. Continuations of the Ti spectrum recorded at an ion beam energy of 10 MeV. (**a**) continues Figure 7b, (**b**) continues Figure 8a.

Figure 9 demonstrates the flavor of the problem. Owing to the typical level structure with, say, triplet levels lying lower than singlet levels, the intercombination decays typically have longer wavelengths than the corresponding resonance lines. The prompt spectrum in Figure 9a is of a wavelength range beyond the range of the prominent lines of Figures 6–8. Many rather weak lines appear, but none of the lines in the spectrum of Figure 9a can be identified from reference tables. Spectrum (b) represents an observation of a 1 mm long section of the ion beam about 5 mm away from the foil. In a delayed spectrum such as in Figure 9b, several intercombination transitions can be recognized in principle, but the line intensity is so low that observations require wide spectrometer slits for sufficient signals, and detection may be challenged yet. The Ti XI line is the $3s^2\ {}^1S_0$–$3s3p\ {}^3P^o_1$ transition in the Mg-like ion. It benefits from cascade repopulation, which is enhanced by a funneling effect of the cascades in the triplet term system. The $3s3p\ {}^3P^o_1$ level is predicted to have a lifetime of about 40 ns (see [87]). In the Al-like ion, there are five lines of the Ti X $3s^23p\ {}^2P^o_{1/2,3/2}$–$3s3p^2\ {}^4P_{1/2,3/2,5/2}$ transition array. The ${}^4P_{5/2}$ level is more highly populated than the other two owing to the statistical weight $(2J+1)$, and its decay is unbranched. Lifetime predictions for this level run to the order of 300 ns (see [87]). The $J = 1/2$ level should have a lifetime about a factor of $1/3$ shorter, and the $J = 3/2$ level lifetime a factor of about three longer, and, for both levels, the decays are branched. Thus, each decay branch is individually weak. The signal that is in principle available per ion charge state is distributed over several levels and their decay channels; the signal is furthermore spread out over a longer flight path. This combination reduces the expected individual line intensities for the Ti X intercombination lines by about two orders of magnitude compared to the single intercombination line in Ti XI. The line pair $3s^23p\ {}^2P^o_{1/2}$–$3s3p^2\ {}^4P_{1/2}/3s^23p\ {}^2P^o_{3/2}$–$3s3p^2\ {}^4P_{5/2}$ has been seen clearly in heavier ions; the latter line is dominant, whereas the former one is a mere companion. This characteristic line pair differs from the broad structure seen here at 62.5 nm. It is likely that the observed structure originates from the Ti VIII 4f–5g transition array, which in a hydrogenic approximation is predicted at a wavelength of 63.28 nm. The Ti VIII transition array dominates the blend with the two Ti X intercombination transitions. An observation of the latter would require a much farther distance from the foil to enable a longer delay after excitation, when the yrast transition and its decay curve tail have practically died out.

In the Si-like ion, there are two decay branches of the lowest quintet level, Ti IX $3s^23p^2\ {}^3P_{1,2}$–$3s3p^3\ {}^5S^o_2$. The upper level lifetime can be estimated near 500 ns (see [87]). The term systems of the Si-like ions are more complex than those of Mg- and Al-like ions, and there is no notable cascade chain than would preferentially repopulate that quintet level. Consequently, the two intercombination lines are not prominent, although the ion beam energy of 8 MeV should favor the Si-like ion over Al- and Mg-like ions. The intercombination transition rates scale steeply with the charge of the ion core (with about the seventh power of the partly shielded ion core charge for these intra-shell transitions). Thus, it is somewhat easier to observe these intercombination lines in heavier elements such as Fe, Ni, or Cu (see examples below).

In Figure 9b, there also are leftovers of yrast transitions. Their upper levels are short-lived (lifetimes below 100 ps), but they are replenished by a chain of cascades from higher-lying yrast levels.

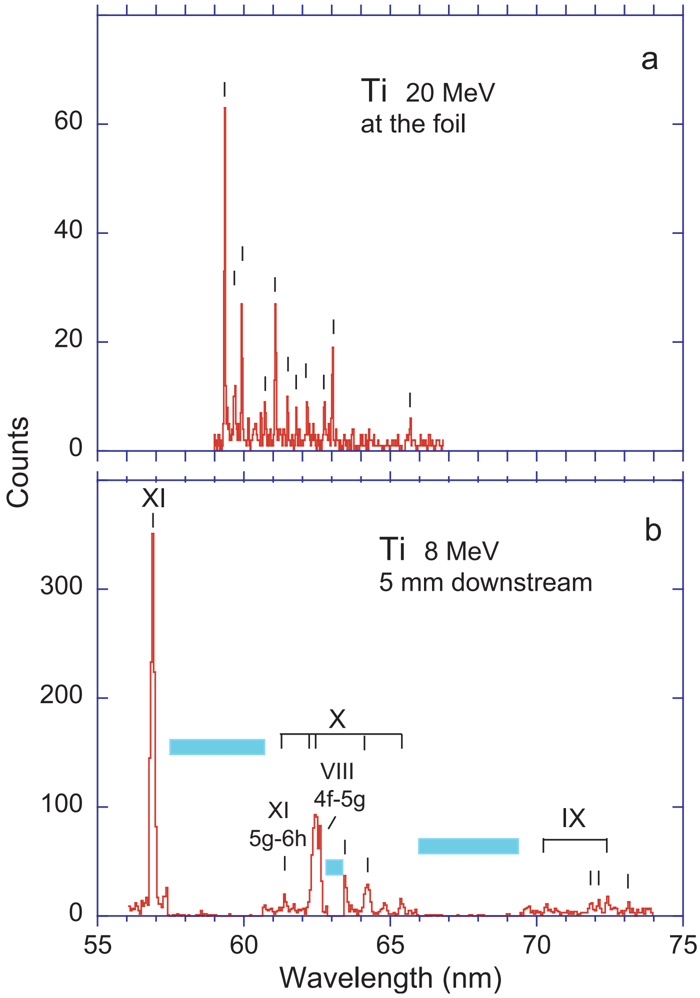

Figure 9. Beam–foil spectra of Ti recorded at ion beam energies of (**a**) 20 MeV and (**b**) 8 MeV. Grating 600 L/mm, line width (FWHM) 0.045 nm in (**a**) and 0.15 nm in (**b**). The strongest lines are identified by the spectrum number. The charge state distributions are close to those of Figure 1b. The light blue horizontal bars mark ranges of data recording with a reduced ion beam charge preset per channel. Spectrum (**a**) has been recorded right after excitation; spectrum (**b**) corresponds to a delay of about 880 ps.

Thus far, we have presented spectra of foil-excited Ti ions up to ion beam energies of 20 MeV. Figure 10 shows a spectrum of the range 19 to 28 nm, recorded at an ion beam energy of 24 MeV. The charge state distribution is centered on $q = 11+$ and $q = 12+$, and ion charge states $q = 9+$ to $q = 15+$ are expected to contribute. Much of the spectrum is rather similar to Figure 3, but now there are all three 4f–5g transition arrays of Ti XII to Ti XIV present in the survey spectrum of Figure 10a. At the present spectral resolution, the Ti XII 4f–5g (Na-like ion) transition array looks almost like a single line, Ti XIII 4f–5g (Ne-like ion) resembles a narrow structure with two major fine structure components, and, in the F-like ion Ti XIV, the 4f–5g array appears as a partly resolved wide multi-line cluster. Near a wavelength of 20 nm, the Ti XIII 3d–4f transition array shows in a second diffraction order. This array has been discussed by Jupén et al. [83].

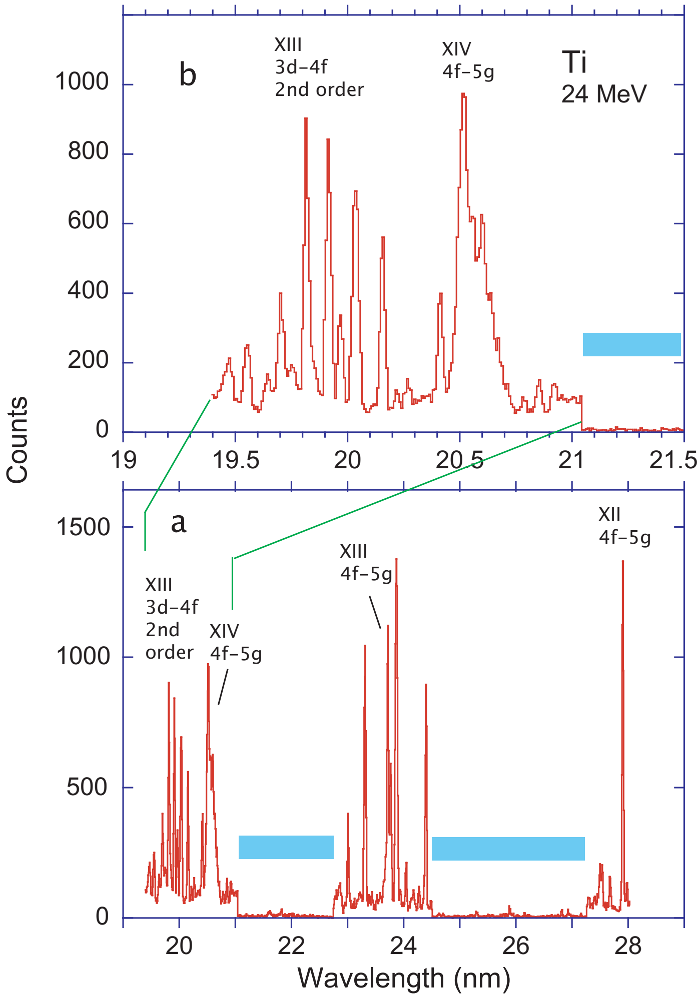

Figure 10. Beam–foil spectra of Ti at an ion beam energy of 24 MeV. Grating 600 L/mm, line width (FWHM) 0.030 nm. The charge state distribution is centered on $q = 11+$ and $q = 12+$, and ion charge states $q = 9+$ to $q = 15+$ are expected to contribute. (**a**) Survey spectrum covering the 4f–5g transition arrays in Ti XII, XIII, and XIV. Near a wavelength of 20 nm, the Ti XIII 3d–4f transition array shows in the second diffraction order. (**b**) This detail has been expanded for the benefit of a comparison with Figure 2.

Figure 11 shows a beam–foil survey spectrum of Ti (in two sections) at an ion beam energy of 24 MeV. Several sections of this data set have served as the basis of annotated spectra in [80]. Unfortunately, those figures have suffered in that journal's procedure for digital archiving. A corresponding spectrum recorded at an ion beam energy of 20 MeV and with a poorer resolution has been presented in [76], together with a simulated spectrum of Ti XIII.

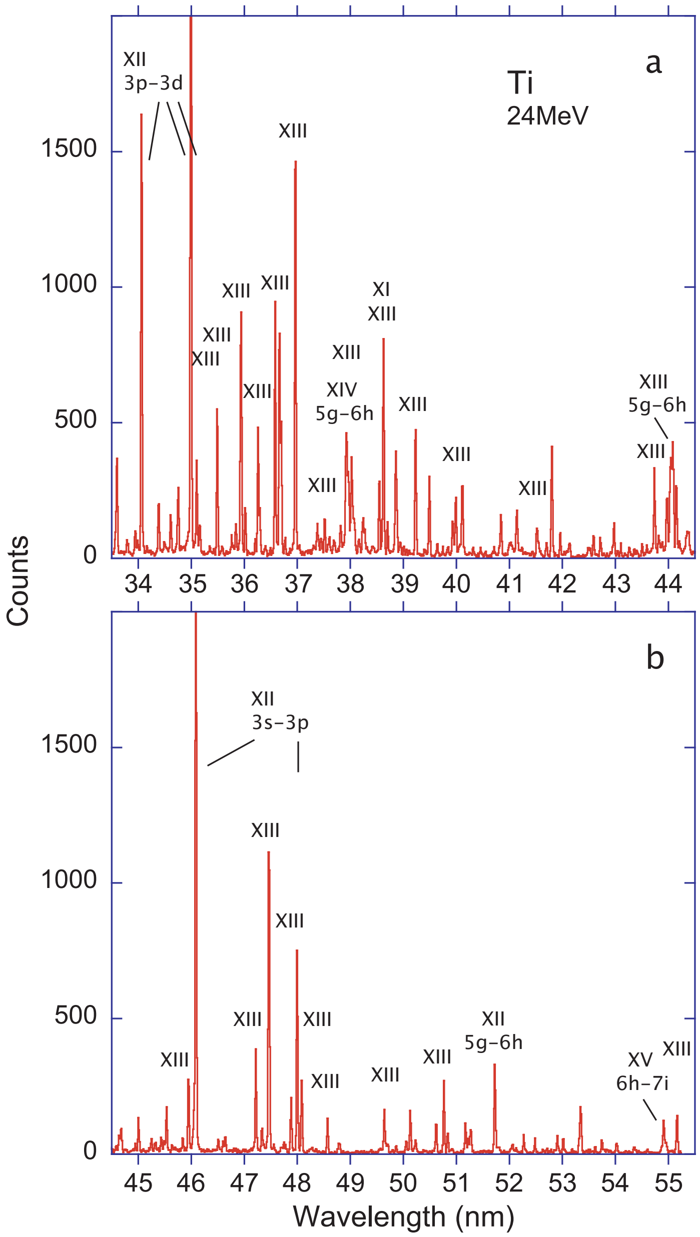

Figure 11. Two consecutive sections of a beam–foil survey spectrum of Ti, recorded at an ion beam energy of 24 MeV. (**a**) ends at a wavelength of 44.5 nm, (**b**) begins at that wavelength. Grating 600 L/mm, line width (FWHM) 0.030 nm. The strongest of the wavelength reference lines of Ne-, Na-, and Mg-like ions are identified by the spectrum number. Several yrast transition arrays are marked.

2.2. *Fe*

Because of the particular prominence of Fe in the EUV spectra of the solar corona and the associated astrophysical interest, Fe has been investigated in many light sources. In the present context of spectra of the iron group elements, a particularly noteworthy group of publications by Del Zanna and (among others) his colleagues Mason, Young, and Storey cover many of the iron ions, benchmarked against the corresponding coronal spectra [88–100]. A laboratory light source that comes close to the ultrahigh vacuum and electron density conditions of parts of the solar corona is the electron beam ion trap (EBIT) [101]. Consequently, EBIT spectra have been used to help interpret solar corona spectra (for example, [24–29,102]. The appearance of the spectra depends on the measurement conditions [103,104], as discussed with examples below. Among the early beam–foil work, there has been a noteworthy activity on the Fe spectra in the Lyon group of Buchet and Buchet-Poulizac and by their colleagues at Caen [105–107]. Jones and Johnson at Brookhaven were among the first to study Fe in the EUV using a multichannel detector system [68,69]. For earlier presentations of Fe beam–foil work at Bochum (much of it done in collaboration with colleagues from Lund), see, for example, [49,50,57–60,75,108,109].

In the beam–foil spectrum in Figure 12, about 90 lines can be discerned by the eye. The same spectrum is presented on a linear and a logarithmic scale in order to help with the orientation in the logarithmic survey spectra discussed later. The spectrometer slits used here were half as wide as in most of our survey spectra (shown previously), and thus the spectral resolution is correspondingly higher. Various line groups that are only partly resolved in the survey spectra can be better disentangled in this spectrum, at the cost (and limitation) of accelerator operating time.

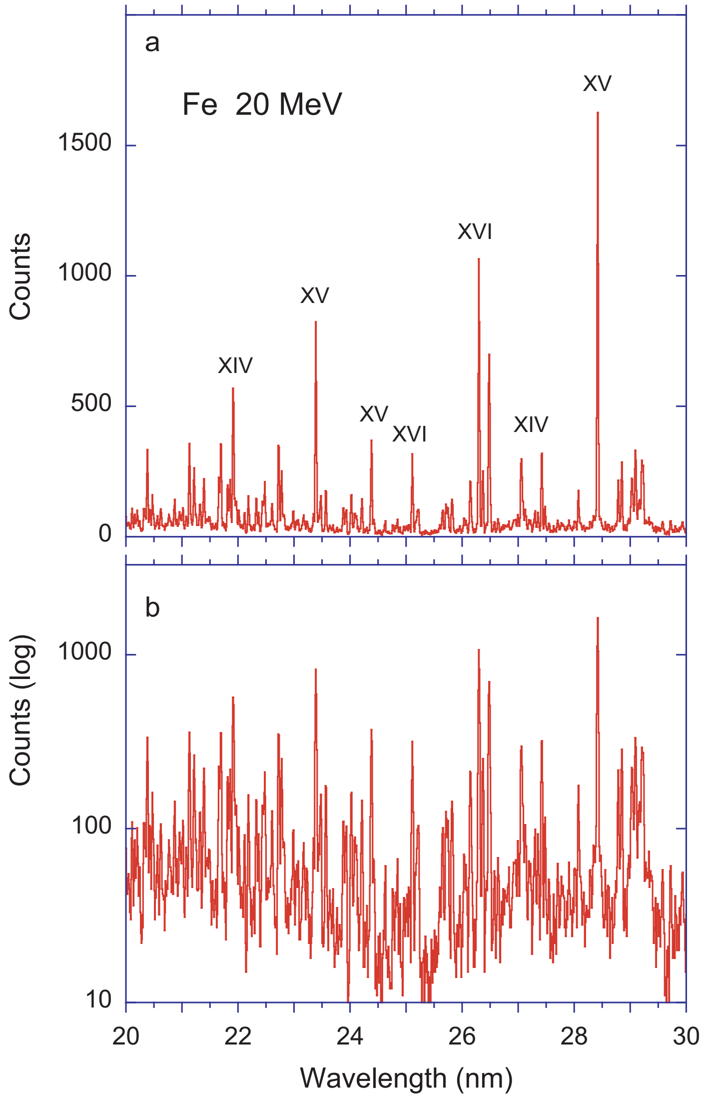

Figure 12. Beam–foil spectrum of Fe at an ion beam energy of 20 MeV in (**a**) linear and (**b**) logarithmic display. Slit width 40 µm, line width (FWHM) 0.03 nm. The strongest lines are identified by the spectrum number. The charge state distribution ranges from $q = 9+$ to $q = 16+$ with a maximum for $q = 12+$ (Fe XIII).

Figure 13 combines two relatively highly resolved beam–foil spectra. About 30 lines can be discerned visually, not all of which are known. For example, the profile of the Fe XVI 3p–3d line at 26.2976 nm [11] suggests a blend with an unknown line, whereas the major contributors to the similarly shaped line at 26.5 nm are known to belong to Fe XIV (26.4785 nm) and Fe XVI (26.5003 nm), respectively. The strongest line in this figure (Fe XV at 28.4164 nm) is neighbored by weaker lines that fall into the wings of the strong line.

Evidently, the spectral resolution of these data is not quite sufficient for separating all the details. However, the spectrometer settings are always a compromise of intended resolving power and affordable operating time. Measurements with a similar spectral resolution as in Figures 12 and 13 have been tried at longer wavelengths too, but the extraction of information suffered from a weaker signal (due to the line intensity distribution in the Fe spectrum, the decreasing efficiency curve of the spectrometer [85]) and the (relatively) higher noise.

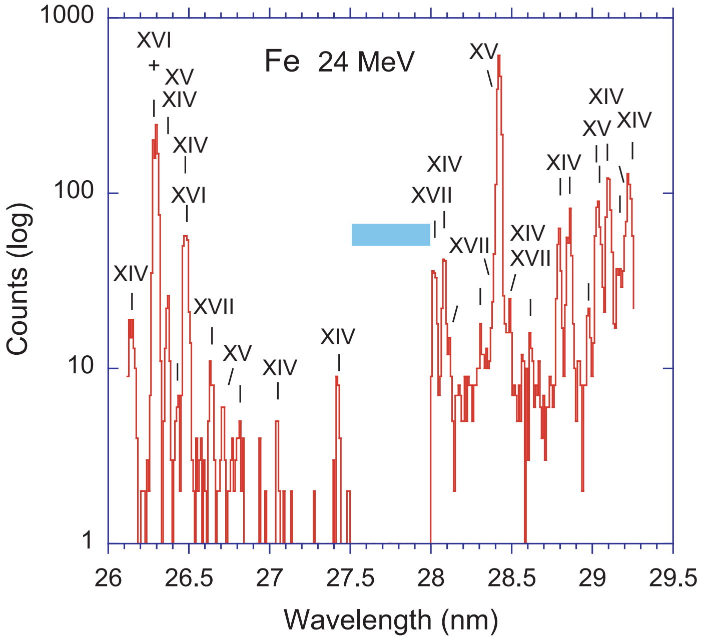

Figure 13. Beam–foil spectra of Fe at an ion beam energy of 24 MeV. Line width (FWHM) 0.03 nm. The strongest lines are identified by the spectrum number. Unidentified lines are marked by a fiducial. The charge state distribution is centered on $q = 13+$, and ion charge states $q = 9+$ to $q = 17+$ are expected to contribute in principle. Two separate measurements have been combined in one plot. The blue horizontal bar from 27.5 nm to 28 nm marks the gap in between.

Figures 14 and 15 juxtapose beam–foil and EBIT spectra (both on log scales). The underlying raw data are the same as presented in [104]. The beam–foil data have been garnered with a scanning grazing-incidence monochromator (grating R = 2.2 m, 600 L/mm) equipped with a channeltron serving as the detector. The experiment required about a day (and night) of accelerator time. The EBIT experiment [28,29] used a grazing-incidence flat-field spectrograph (variable line-spacing grating of R = 5 m and approximately 1200 L/mm) [110,111]; the spectrum was recorded on a CCD chip with an exposure time of 30 min. The spectrograph has no entrance slit but images the 60 µm wide zone of the stored ion cloud exposed to the energetic electron beam directly onto the detector. The CCD chip has an intrinsic background with some structure that further modeling might reduce in the presentation. However, the signal-to-noise ratio of both measurements is of the same order of magnitude, with the EBIT recording being much faster. The spectrograph grating used shows the second order of diffraction images well; the spectrograph was set for observation of the 20 nm to 44 nm wavelength range in the first order. Spectroscopically, the two spectra are rather similar; the line width of the scanning monochromator is constant as a function of wavelength, whereas, with the flat-field spectrograph, it is slightly smaller in the wavelength range of Figure 14 and increasing towards long wavelengths. This may partly be a result of imperfect focusing but is mostly a consequence of the flat image field being a very good, but imperfect approximation. The focal curve of variable line spacing gratings as used in flat-field spectrographs is intentionally distorted from the basic Rowland circle perimeter to feature a straight section that can be matched by a flat detector chip. The technical specification by the manufacturer (Hitachi) of the grating used in the aforementioned flat-field spectrograph states a wavelength working range from 5 nm to 20 nm. For the electron beam ion trap spectra of Fe and Ni (below), the spectrograph was set to monitor the wavelength range from 20 nm upwards, which is fully outside the manufacturer-specified operating range. Evidently, the focusing works well beyond the prescribed wavelength range, but for wavelengths longer than some 35 nm, the line images become increasingly wider.

The important differences between the beam–foil and EBIT spectra in Figures 14 and 15 concern the physical conditions in the light source. Beam–foil spectra contain practically electric dipole (E1) transitions only because of the inherent time resolution and the typical level lifetimes. The excitation differs between beam–foil interaction at a high (solid-state) electron density and the electron impact excitation at very low electron density in an electron beam ion trap (which resembles excitation by Maxwellian electrons in the dilute gas of the solar corona). Consequently, in an EBIT, most of the level population is in the ground configuration, whereas, in the ion–foil interaction, the excitation reaches a high level and then the population pours down in cascades. The massive differences in the spectra have been demonstrated in [103,104]. Astrophysical plasmas can contain all elements at once, whereas the laboratory ion beam is elementally pure. The EBIT is in between; in the EBIT experiment with Fe, injection of ironpentacarbonyl ($Fe(CO)_5$) was used, which disintegrates when hit by the electron beam in the trap, hence the spectra may comprise emission from C, O, and Fe ions. The heaviest ions are trapped best (and reach the highest charge states), which leaves Fe as the strongest contributor to such a spectrum. The strong Fe EUV lines Fe IX near 17.1 nm, Fe X near 17.45 nm (see [25]), Fe XII near 18.7 nm, Fe XII near 19.4 nm (see [26]), Fe XIII near 20.3 nm, Fe XIV near 21.1 nm (see [27]), etc. show up in their second diffraction order positions, as well as the strong O VI lines at 15.0 nm, 17.3 nm, and so on.

A wavelength range near 21 nm has been investigated at the Livermore EBIT in detail in [27], using a high resolution spectrograph [112]. A further section of the high-resolution spectrum has been added recently [113]. The wavelength interval 28–35 nm investigated with a medium resolution spectrograph has been discussed in [28,29]. In this wavelength band, the difference between the high-electron density excitation in the beam–foil interaction (Figures 14a and 15a) and the excitation by a low-density electron beam (Figures 14b and 15b) is particularly striking. The ion charge states present in both data sets are rather similar, but the relative emission signal of certain types of levels is much stronger in the foil-excited ion beam [104].

Figure 16 shows samples of prompt and delayed spectra of foil-excited Fe ion beams. In Reference [31], it has been discussed how the isotope-pure beam–foil light source suffers from a scarcity of wavelength reference lines in many spectra, especially in delayed ones. In prompt spectra (with reference lines), the signal of the decays of long-lived levels is too weak to be seen against the competition by short-lived level decays. Away from the exciter foil, after suitable delays, the ‘slow’ decays that have ‘survived’ become dominant, but the reference lines have died out. The spectra in Figure 16 demonstrate a pathway to calibrate delayed spectra (b,c) that have no lines in common with the prompt spectra (in a) that have known reference lines. However, the changes of a heavy-ion accelerator to a different ion beam energy imply small uncertainties in the ion beam trajectories, which cause uncertainties in the Doppler correction in the observations of a fast ion beam, on top of the limited mechanical reproducibility of a scanning monochromator as was used here. The lines seen in the prompt spectrum can easily be recorded with high statistical reliability. The lines observed in the delayed spectra are statistically much poorer, in addition to the larger line widths caused by wider spectrometer slits necessitated by the scarce signal. In the delayed spectra, a number of line positions have been marked by visual inspection. Owing to the line width, many lines overlap with their neighbors, and more blends are expected. Computations have been undertaken [59] to identify the many intercombination transitions expected in S- and Cl-like ions. Many of the suggested candidates are labeled in

Figure 16b,c. The spectral feature at 25.7 nm is expected to consist of three components with different lifetimes. This complexity suggests that the present classifications [59] have to be considered as preliminary until better resolved data of higher statistical reliability and at further time steps become available, as well as accurate computations for all charge states expected. Recent ab initio computations (such as [32–34,36–44,114]) appear to be on the right path and reach an accuracy that is about an order of magnitude higher than what was available at the time of the beam–foil experiments described here.

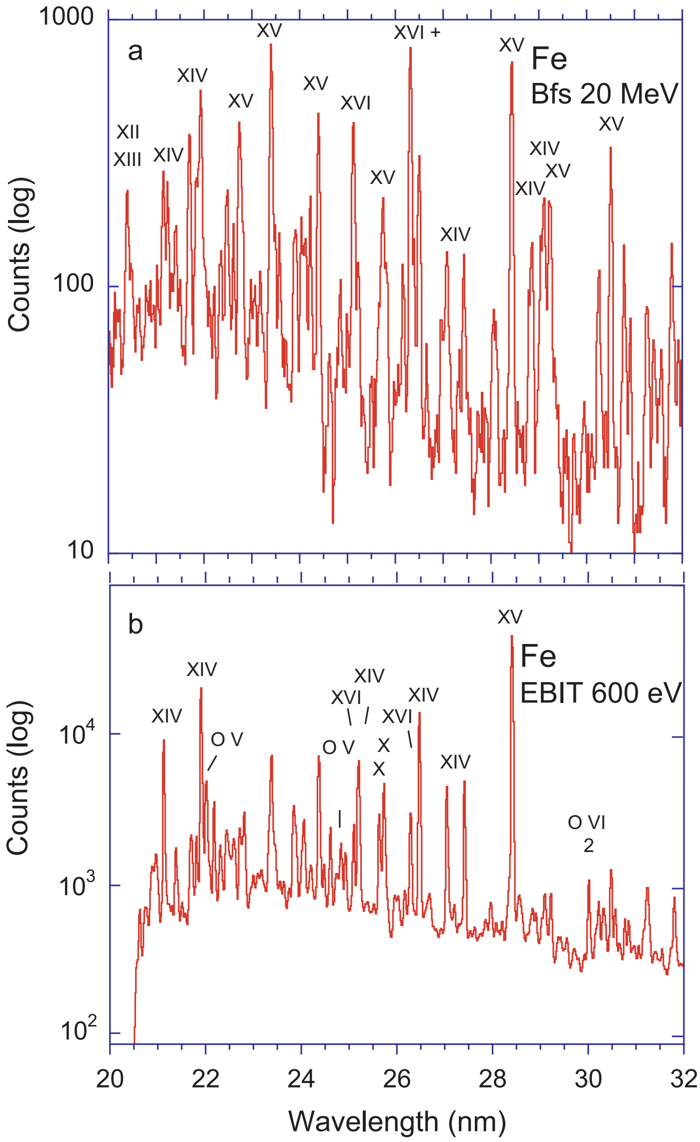

Figure 14. Fe spectra observed with (**a**) the beam–foil light source [104] and (**b**) in an electron beam ion trap (see [28,29]). The beam–foil spectrum of Fe has been recorded at an ion beam energy of 20 MeV. Slit width 80 µm, line width (FWHM) 0.06 nm. The charge state distribution is centered on $q = 11+$, and ion charge states $q = 8+$ to $q = 14+$ are expected to contribute. The EBIT spectrum has been obtained at an electron beam energy of 600 eV. The strongest lines are identified by the spectrum number. Line labels including an Arabic numeral '2' indicate a line in second diffraction order; several O V and O VI lines appear and serve for wavelength calibration.

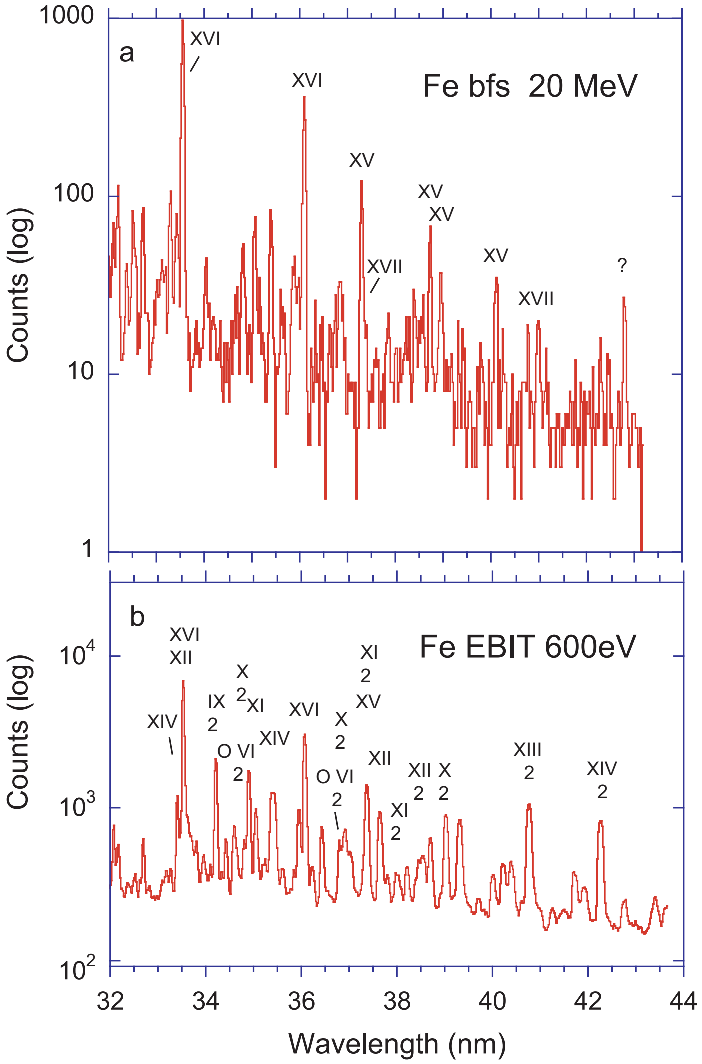

Figure 15. Fe spectra observed with (**a**) the beam–foil light source [104] and (**b**) in an electron beam ion trap (see [28,29]). The beam–foil spectrum of Fe has been recorded at an ion beam energy of 20 MeV. Slit width 80 µm, line width (FWHM) 0.06 nm. The charge state distribution is centered on $q = 11+$, and ion charge states $q = 8+$ to $q = 14+$ are expected to contribute. The EBIT spectrum has been obtained at an electron beam energy of 600 eV. The strongest lines are identified by the spectrum number. Line labels including an Arabic numeral '2' indicate a line in second diffraction order; several O V and O VI lines appear and serve for wavelength calibration. (**a**) continues Figure 14a, (**b**) Figure 14b.

The measurement problem is further discussed below in the section on Ni. There is a transition in the the Si-like ion, Fe XIII $3s^2 3p^2\ {}^3P_2$–$3s^2 3p3d\ {}^3F^o_3$ [96], at a wavelength of 23.903 nm that appears at ion beam energies between those of Figure 16a,b and at delays shorter than that of Figure 16b [50]. This line has been recognized in spectra of the solar corona, where its wavelength can be measured more accurately than in the delayed beam–foil spectra, and, therefore, its wavelength may then be used to calibrate the latter.

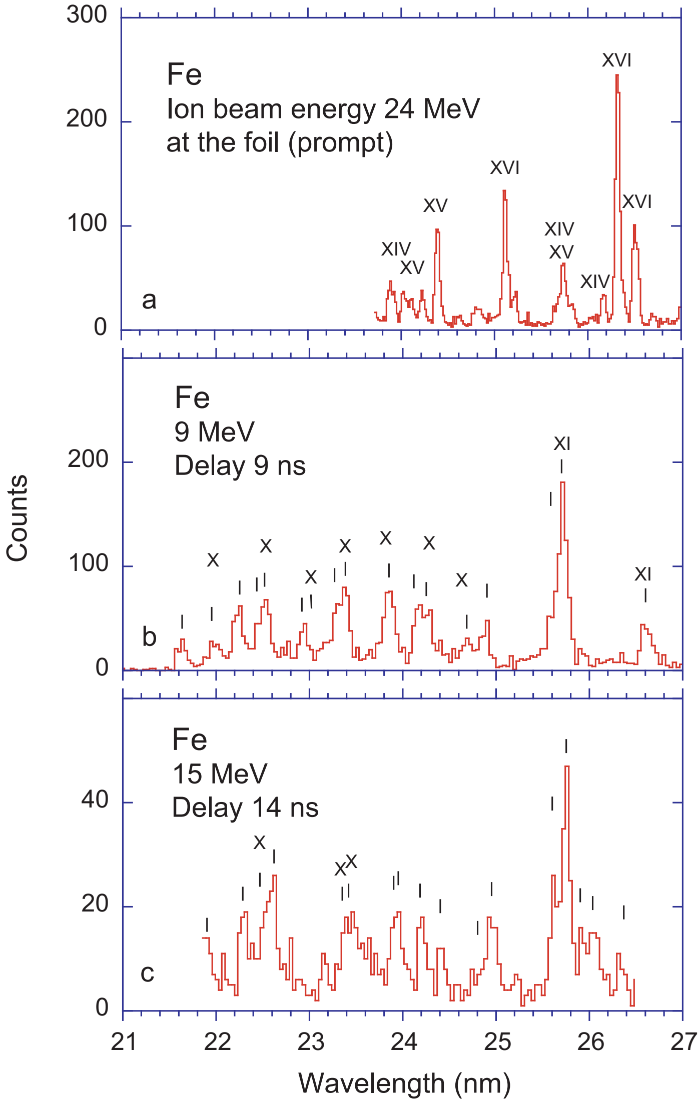

Figure 16. Prompt and delayed beam–foil spectra of Fe at various ion beam energies. The strongest lines are identified by the spectrum number (based on [59]). Unidentified lines are marked by a fiducial. The charge state distribution is centered on $q = 11+$, and ion charge states $q = 8+$ to $q = 14+$ are expected to contribute. (**a**) Observation at the foil, slit width 80 µm, line width (FWHM) 0.06 nm; (**b**) Observation of the ion beam 50 mm downstream of the foil, corresponding to a delay of 9 ns after the spectrum in (**a**). Slit width 150 µm, line width (FWHM) 0.12 nm; (**c**) Observation of the ion beam 100 mm downstream of the foil, corresponding to a delay of 14 ns after the spectrum in (**a**). Slit width 120 µm, line width (FWHM) 0.09 nm.

2.3. Ni

Ni is less abundant than Fe but not drastically so. Thus, it is of high astrophysical interest. A problem lies in the fact that Fe and Ni emissions populate overlapping spectral ranges. Therefore, the spectral diagnostics of stellar plasmas, in which both elements are present, require information on both elements and their spectra. Partial beam–foil spectra and decay curves of highly charged Ni ions have been evaluated previously (see [55,56,115–119] and several multi-element papers cited above).

Examples of three topics are discussed here:

(a) moderately highly resolved prompt spectra and slightly delayed spectra in the range from 14 nm to 23 nm,

(b) comparison of beam–foil and EBIT spectra in the range 20 to 44 nm, and

(c) survey spectra recorded with a delay to enhance the visibility of decays of long-lived levels; 3s–3p and 3p–3d intercombination decays.

Figure 17 shows two moderately highly resolved spectra: a prompt spectrum and a slightly delayed spectrum in the wavelength range 14–23 nm. These data have been presented before (see Figures 4 and 5 of reference [56]);

they are shown again for the context of this discussion and to indicate some progress of the identification process. At the time, the recording of delayed spectra was started as a tool to reduce the complexity of the observed spectra. The prompt spectrum in Figure 17a is so line-rich that, in the wavelength interval between 15 nm and 22 nm, many lines merge into a wide hump. Actually, at the time of the experiment, none of the lines in the hump could be identified. In the various delayed spectra then recorded (for an example, see Figure 17b), much of the spectral hump was gone and thus recognized as having originated from a plethora of decays from possibly multiply excited and hence short-lived levels. However, incidental line blends were still frequent and attempts at identification failed. Later work at significantly longer delays (up to some 20 ns, the maximum feasible with the given vacuum chamber size) and at various ion beam energies revealed that the wavelength range from 17 nm to 26 nm comprises the 3p–3d intercombination decays in Si- to Ar-like ions of Ni [119]. The aforementioned newer computations of many of these ions [37–44,114] might support fresh attempts at line classification in delayed spectra of this wavelength range. Moreover, many of the lines in the prompt spectra longwards of the hump can nowadays be identified with information from considerably augmented spectral data bases [11].

A key to the analysis of the prompt spectrum in Figure 17a is the line just above 22 nm in wavelength, which has meanwhile been identified with the Ni XVIII $3p_{1/2}$–$3d_{3/2}$ transition at 22.0424 nm [11]. This is a rather weak line in this spectrum because the Na-like ion charge state is barely produced at an ion beam energy of 24 MeV. However, the line is clean enough to serve as a reference wavelength anchoring the wavelength scale in the measurement. Based on this line identification, a number of further identifications can be made by wavelength, based on the NIST ASD database [11]. The NIST data base lists many more transitions in the wavelength range of Figure 17, but, at the present experimental settings and conditions, there are many line blends to consider. Therefore, Figure 17a identifies only ten spectral features with spectrum numbers. Note that the 22-nm line has practically died out by the time delay of Figure 17b, although the upper level is readily repopulated by radiative cascades. Note also that the strongest line in the delayed spectrum, near 21.01 nm, has an amplitude of about 100 counts. It is likely to originate from the decay of a long-lived level. The signal of this line, retro-estimated for the position of the foil, would not be much higher than 100 counts, and thus the line makes up part of a weak line blend there but not more. Consequently, the two spectra have no clean lines in common, and the wavelength scale of the delayed spectrum rests on the mechanical reproducibility of the spectrometer drive alone. This measurement uncertainty is estimated here as ±0.015 to 0.02 nm. This leaves the aforementioned problem: There is no wavelength reference found yet that would tie the wavelength scales of the downstream measurements directly to well known lines in the prompt spectra, and thus a wavelength uncertainty caused by the properties of the spectrometer drive limits the measurement accuracy. To bridge this gap, beam–foil spectra of Ni with short delays of only 0.1 to 0.2 ns (to suppress some blends with short-lived level decays while exploiting the cascade feeding of reference lines) might offer a path forward.

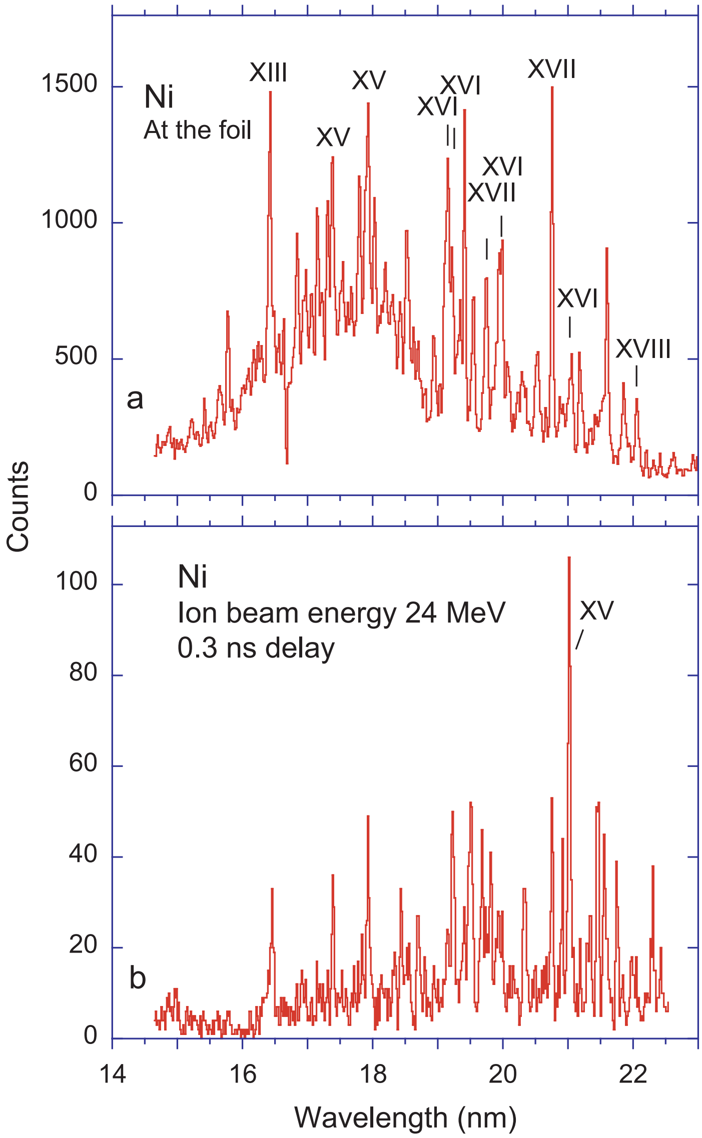

Figure 17. Beam–foil spectra of Ni at an ion beam energy of 24 MeV. Slit width 60 µm, line width (FWHM) 0.045 nm. The charge state distribution peaks near q = 13–14+, and ion charge states $q = 10+$ to $q = 18+$ are expected to contribute. The figure refers to the same raw data as Figure 5 of [56]. (**a**) Observation at the foil; (**b**) Observation of the ion beam 3 mm downstream of the foil, corresponding to a delay of about 0.3 ns after the spectrum in (**a**).

An alternative approach is an accurate computation of suitable reference lines for delayed spectra, which for a long time has been lacking. The strongest line in the delayed Ni spectrum has previously been identified with guidance from much earlier Hartree–Fock calculations [120] and technically with the charge state distribution changing as a function of ion beam energy as originating from the Si-like spectrum (Ni XV) (see Figure 2 of [56]). In a set of line identifications in the solar corona, based on such delayed beam–foil spectra [60], the transition was identified as $3s^23p^2\ {}^3P_2$–$3s^23p3d\ {}^3F^o_3$. It has not been possible yet to associate this transition with any solar corona emission line as reported by Dere [121]. Unfortunately the Ni XV line appears to be too weak to show in the *Hinode*/EIS spectra [122], so that a good solar wavelength value is not yet available. Interestingly, this line has been seen in the Livermore electron beam ion trap, at a wavelength of 21.013 ± 0.002 nm [27], which appears to be the most accurate measurement so far. Computations by ab initio techniques employed by Vilkas and Ishikawa [38] have yielded a wavelength value of 21.015 nm that is much closer to measurement than the earlier semi-empirically scaled computations. The even more recent computations by Jönsson et al. [39] have reached a comparable accuracy (and an almost identical wavelength result of 21.013 nm in this case). However, the agreement of computations with each other is no proof, nor is a single data point agreement with an experimental result that involves the aforementioned calibration limitations. The closest element for which solar coronal data offer a match is Fe (see [60]). At the time, the association was based on the comparison of a known to be not quite accurate theoretical isoelectronic trend with not yet assigned lines in the solar spectrum. The ab initio multi-reference Møller–Plesset computations of the Ishikawa group [37,38] corroborated the tentative astrophysical line assignments and the beam–foil identifications for a sequence of elements. A decade later, Jönsson et al. [39] applied a different computational approach and obtained almost identical results. Table 1 recapitulates the work on the $3s^23p^2\ ^3P_2$–$3s^23p3d\ ^3F^o_3$ transition in Si-like ions.

Table 1. Computed and measured wavelength results (in nm) on the $3s^23p^2\ ^3P_2$–$3s^23p3d\ ^3F^o_3$ transition in Si-like ions. Solar data refer to [121]; Bfs data have been obtained by beam–foil spectroscopy as explained in the text; EBIT data have been obtained at an electron beam ion trap.

Element	Z	Theory 1986 [120]	Experiment	Uncertainty	Light Source	Theory 2004 [38]	Theory 2016 [39]
Ca	20	40.299	40.455	0.003	solar		
Sc	21						
Ti	22	32.629	32.786	0.003	solar		32.878
V	23	29.837					30.041
Cr	24	27.486	27.660	0.003	solar	27.666	27.665
Mn	25	25.496				25.646	25.642
Fe	26	23.77	23.903	0.003	solar	23.905	23.894
			23.92	0.015	Bfs		
Co	27	22.251	22.38	0.015	Bfs	22.367	22.365
Ni	28	20.911	21.02	0.015	Bfs	21.015	21.013
			21.013	0.002	EBIT		
Cu	29	19.73	19.83	0.02	Bfs	19.807	19.806
Zn	30					18.721	18.720

It is good to find that the purely experimental approach with the aforementioned technical limitations has found a significant and unblended line in the delayed spectrum, the wavelength of which agrees well with accurate computations. The reliability of the latter for this $3s^23p^2\ ^3P_2$–$3s^23p3d\ ^3F^o_3$ transition is better than ±0.01 nm and clearly surpasses the present experimental uncertainty. Unfortunately, a computation found to yield excellent results in one case is not guaranteeing the same high quality in others, as evidenced by the differences between computational results for several elements. Most lines in this kind of delayed spectra belong to ions with a more than half filled valence shell (P-like, S-like, etc.), and that increases the complexity of the problem. However, these computations have at least some excellent results to their credit. It should therefore be feasible to identify many more lines in the delayed spectra at the present level of experimental and computational accuracy.

As mentioned above in the subsection on Fe, high-resolution nickel spectra have been recorded at the Livermore electron beam ion trap EBIT (see, for example, [27]). The spectrograph used [112] produced highly resolved spectra of wavelength bands that matched the individual detection bands of the *SolarDynamicsObservatory* spacecraft, but it did not permit observation beyond wavelengths of about 25 nm, where a smaller, medium-resolution flat-field spectrograph [110,111] was employed instead [28,29]. The spectra obtained with this instrument are close in resolution to the beam–foil survey spectra of Ni [56] that have been discussed above. It seems appropriate to inter-compare the beam–foil and EBIT Ni spectra in their wavelength range of overlap, 20–44 nm (see Figures 18 and 19, at the same spectrograph settings as for Figures 14 and 15). Since Ni is introduced into the ion trap as nickelocene ($Ni(C_5\,H_5)_2$), there are no second order calibration lines of oxygen in this spectrum, in contrast to Fe (see Figures 14b and 15b). The line of Ni XV near 21.0 nm that provides a key to the interpretation of the delayed beam–foil spectrum in

Figure 17b appears as one of the weaker lines in the EBIT spectrum of Figure 18b, alongside many other Ni lines, most of which are known [11]. As mentioned in the discussion of Fe data, the electron beam ion trap camera signal appears on a thermal background (at cryogenic temperature), but on a basis of equal measurement time, the signal-to-noise ratio is much better than with the scanning monochromator and its channeltron detector. Both experiments and detection systems produce and reach about the same charge ions, but the excitation differs drastically. In the ion–foil interaction at high electron density, the level population depends very much on the statistical weight of the upper level and on cascade repopulation, while, in the low electron beam ion trap, the excitation is beginning largely from ground state ions (see [103,104]). This difference is recognizable in the present Ni spectra by significantly different relative line intensity ratios.

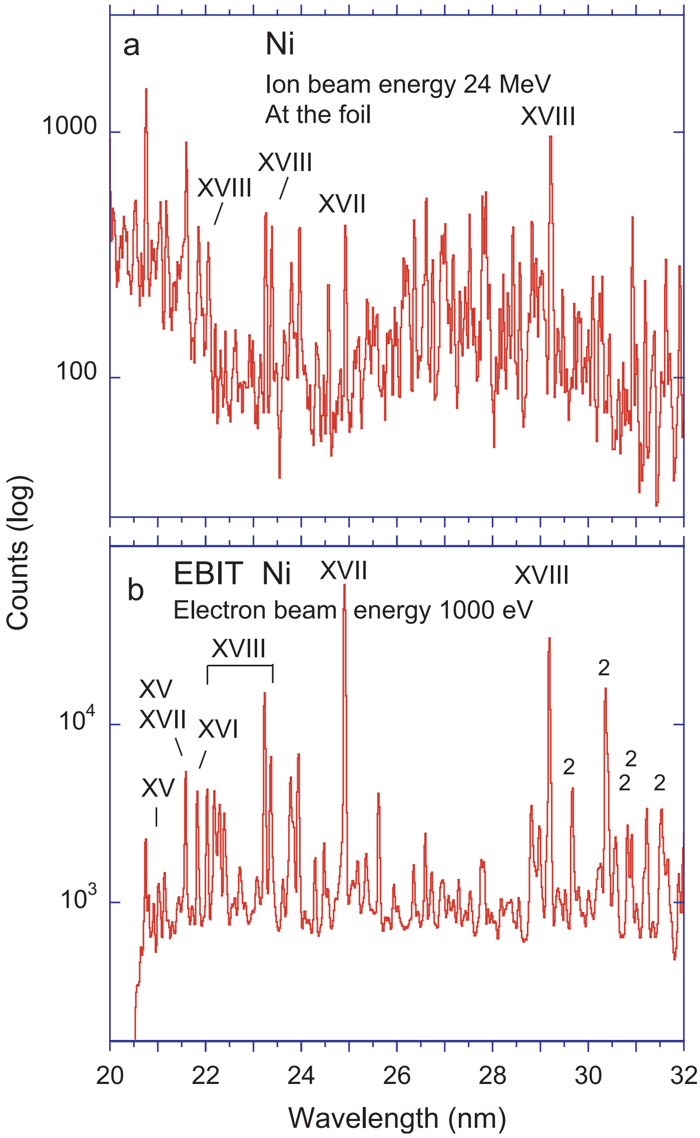

Figure 18. Spectra of Ni in two different light sources. (**a**) Beam–foil spectrum at an ion beam energy of 24 MeV. Line width (FWHM) 0.045 nm. Several of the strongest lines are identified by the spectrum number; (**b**) electron beam ion trap spectrum at an electron beam energy of 1 keV. The flat-field spectrograph setting is the same as used for the spectra in Figures 14 and 15. Line markers with an Arabic '2' indicate second diffraction order images.

In the EBIT part of Figure 19, a feature already discussed in Figure 15 (on Fe) recurs: besides the rather narrow lines from the first diffraction order images, the long-wavelength section shows a number of wider lines with smooth profiles indicative of a good statistical reliability. Many of these lines are the second-diffraction order images of prominent resonance transitions in Ni XII and higher, whose wavelengths fall into the range 15 nm and higher, that is, the first-diffraction order images lie outside the present image field. The notable widening of the spectral lines in the long-wavelength part of the EBIT spectrum is a result of the geometry of flat-field spectrographs (as explained in the Fe section above); the spectrograph wavelength setting used here is outside the grating manufacturer's suggested operating range. Owing to the inherent shift of similar transitions from Fe ($Z = 26$) to Ni ($Z = 28$) to shorter wavelengths, the first-diffraction order lines detected in the EBIT spectrum of Ni fall mostly into Figure 18b and only a small part into Figure 19b. Hence, the second-order lines happen to dominate Figure 19b. Nevertheless, there are a number of first-diffraction order lines at the longer wavelengths, and some of them appear more strongly in the EBIT spectrum than in the spectrum from the foil-excited ion beam.

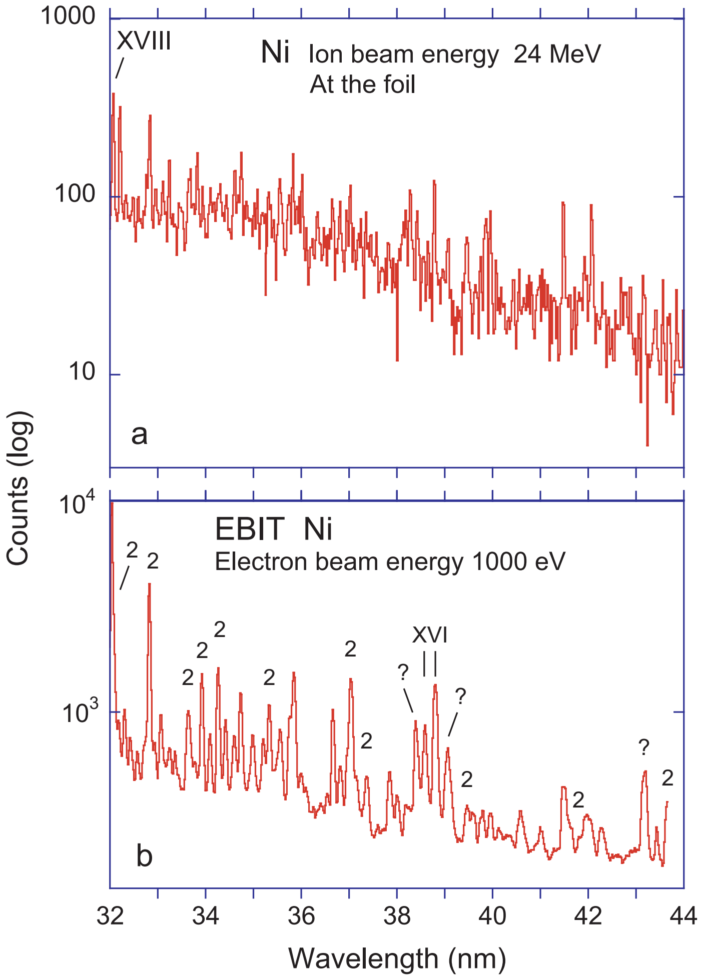

Figure 19. Spectra of Ni in two different light sources. (**a**) Beam–foil spectrum at an ion beam energy of 24 MeV. Line width (FWHM) 0.045 nm. Several of the strongest lines are identified by the spectrum number; (**b**) electron beam ion trap spectrum at an electron beam energy of 1 keV. The flat-field spectrograph setting is the same as used for the spectra in Figures 14 and 15. Line markers with an Arabic '2' indicate second diffraction order images. (**a**) and (**b**) continuation Figure 18a,b, respectively. Line markers with an arabic '2' indicate second diffraction order images.

Figures 20 and 21 show survey spectra that have been recorded with a delay after the excitation in order to enhance decays of long-lived levels, such as the 3s–3p and 3p–3d intercombination decays. Because the signal rate in such delayed spectra is intrinsically much lower than that in prompt spectra, the measurements could only be afforded at the Bochum tandem accelerator laboratory with its capability of uncommonly high ion beam currents. Individually, the spectra might be seen as not very exciting and of rather poor signal-to-noise ratio. The combination shows how reproducible even seemingly weak spectral features are, for example in the wavelength interval 30–32 nm. The upper spectrum shows a group of four lines at a delay of 2 ns, of which two survive till the lower (delayed) spectrum at 10 ns. In this wavelength band lie several Ni XVIII lines (3s–3p transitions near wavelengths of 29 nm and 32 nm, respectively), the upper levels of which are not very long lived but are replenished by cascades. Near 25 nm, the Ni XVII resonance line can similarly be discerned, and also a 3s–3p transition with cascade feeding.

The green bands in Figures 20 and 21 mark wavelength ranges in which the spectra reveal significant line emission from long-lived levels. From 17.5 nm to about 26 nm is the range of the 3p–3d intercombination transitions from the decay of long-lived levels. At a delay of 2 ns, the spectrum is dominated by the 21-nm line in Ni XV that has been discussed above, but, at 10 ns after excitation, this line has lost its dominance, and another spectral feature near 22.2 nm, a blend of 3p–3d transitions in Ni XV and Ni XVI dominates. In fact, the pattern of relative line intensities has changed in the entire line group, signaling the very different level of lifetimes contributing. One must not forget that the charge state distribution after foil excitation depends on the ion beam energy. At not much lower energies than used for the spectra shown, a strong contribution is expected near 22.6 nm from several intercombination transitions in S-like Ni XIII (see prompt and delayed spectra shown in [56]).

In the wavelength band 36–48 nm, we find several 3s–3p intercombination transitions in Mg- to Si-like ions. These are Ni XVII $3s^2\ ^1S_0$–$3s3p\ ^3P^o_1$ at 36.680 nm, the transition array Ni XVI $3s^23p\ ^2P^o_{1/2,3/2}$–$3s3p^2\ ^4P_{1/2,3/2,5/2}$ (wavelengths 36.85 nm to 43.14 nm), and the Ni XV $3s^23p^2\ ^3P_{1,2}$–$3s3p^3\ ^5S^o_2$ line pair at 41.7 nm and 44.0 nm, respectively. Besides these well-established transitions, there are a few more unidentified candidate lines in this neighborhood (for example, near 43 nm and 46.5 nm). Several further groups of lines of long upper level lifetime have been noted and marked in the long-wavelength section of the delayed spectra. These spectral features (near 51 nm, 54.2 nm, 57.7 nm and 62.7 nm) have not been identified yet. They have not been systematically searched for, but are foundlings in exploratory measurements “looking for what’s there," even as the literature does not know of anything in the area yet.

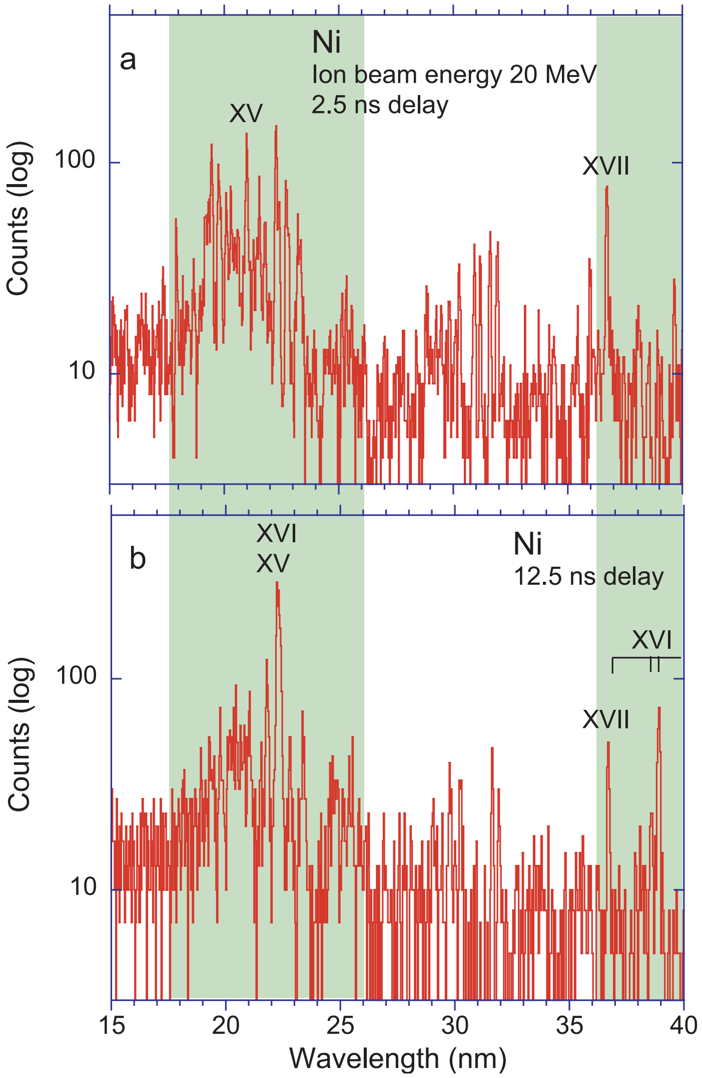

Figure 20. Beam–foil spectra of Ni at an ion beam energy of 20 MeV. (**a**) Observation at a delay of about 2.5 ns after excitation, line width (FWHM) 0.09 nm; (**b**) observation at a delay of about 12.5 ns after excitation, line width (FWHM) 0.11 nm. The strongest lines are identified by the spectrum number. Unidentified lines are marked by a fiducial with a question mark. The charge state distribution is centered on $q = 13+$, and ion charge states $q = 10+$ to $q = 17+$ are expected to contribute. The green bands mark ranges of evident emission by long-lived levels.

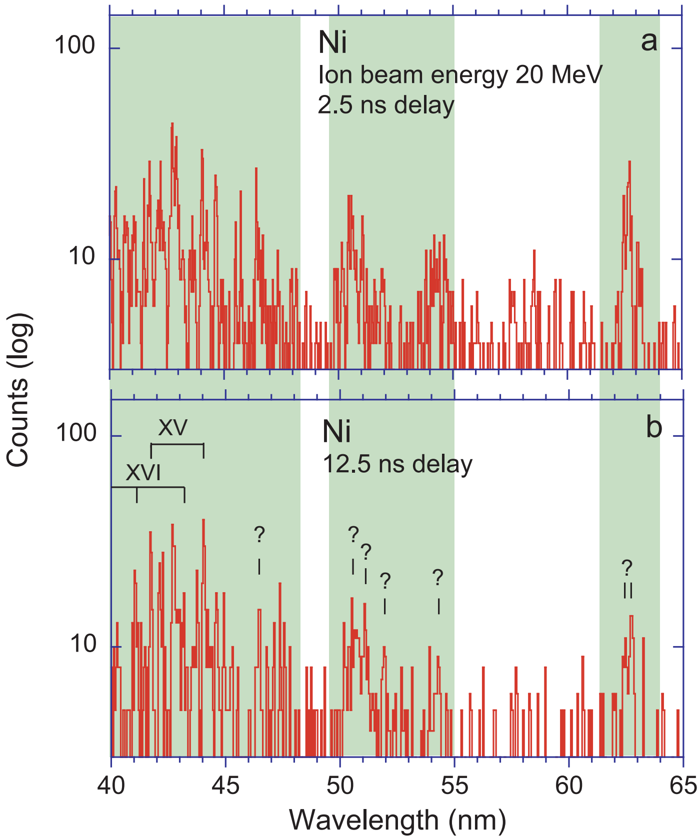

Figure 21. Beam–foil spectra of Ni at an ion beam energy of 20 MeV. (**a**) Observation at a delay of about 2.5 ns after excitation, line width (FWHM) 0.09 nm; (**b**) observation at a delay of about 12.5 ns after excitation, line width (FWHM) 0.11 nm. The strongest lines are identified by the spectrum number. Unidentified lines are marked by a fiducial with a question mark. The charge state distribution is centered on $q = 13+$, and ion charge states $q = 10+$ to $q = 17+$ are expected to contribute. The green bands mark ranges of evident emission by long-lived levels. (**a**) and (**b**) continue the spectra of Figure 20a,b.

2.4. Cu

As an odd-numbered element, Cu is astrophysically not very abundant, and consequently of little interest in that field. However, terrestrial laboratories use Cu conductors and antennas in vacuum chambers, and therefore Cu does appear in spectra of many hot plasmas, intentionally or not. It is about as easy to produce an ion beam of Cu as it is for Ni, and thus the signal rate can be conveniently high in beam–foil experiments.

At an ion beam energy of 36 MeV, the charge state distribution [67] behind the exciter foil peaks at $q = 15+$ (Si-like ions of Cu) and reaches up to $q = 19+$ (Ne-like). This is almost as high (in terms of atomic systems) as 24 MeV for Ti, which has been used to study the F- and Ne-like spectra and level lifetimes of Ti. However, in Ti, this was achieved with $q = 5+$ ions, which are much more abundant in the corresponding charge state distribution at the gas stripper, and thus a much better signal rate resulted. It is easy to see that isoelectronic sequences cannot be studied at will with a given accelerator. Consequently, our studies of iron-group elements aimed at F- and Ne-like ions near Ti, Mg- to Si-like ions for Fe, Ni, and Cu, and ions with more electrons for elements Mn through Zn.

Much of the Bochum beam–foil work on Cu (with emphasis on intercombination transition wavelengths and rates) has already been published. Some of the early presentations of beam–foil survey spectra of Cu (such as in [115]) have suffered from the later digitization for archiving process. In these line-rich spectra, there has been no significant progress towards line identification, and therefore the prompt survey spectra are not shown again. A considerably greater success has been achieved in (delayed) detail spectra such as those of the intercombination decays in Mg- through Si-like spectra [55,56,115,119] and in delayed spectra of Si- to Ar-like ions [59,123]. For Cu, the simple spectra of Na- and Mg-like ions can be produced at the Bochum laboratory only at the performance limit of the accelerator system. It seemed worth trying to make use of the high ion beam current available and record higher-resolution spectra at lower ion beam energies, and consequently the Bochum beam–foil data holdings on Cu have an emphasis on the lower charge state ions.

Figure 22 shows an example, a spectrum with many lines (about 50 are discernible by eye), but with merely two lines marked with a spectrum number. The ion beam energy of 16 MeV is too low to produce any Na- and Mg-like ions with their well-known resonance lines. The literature knowledge (with the example of the NIST ASD database [11]) of the spectra of lower charge states is progressively poorer. Chance coincidences of listed lines and observed features are meaningless, if corresponding other lines of the same spectra cannot be identified as well. Another problem is the wavelength measurement with a mechanically scanning monochromator that needs at least one reference line to ascertain the mechanical shifts of the day. The sample spectrum in Figure 22 is the last part of a sequence of spectra recorded at ion beam energies up to 31 MeV (spectra shown in [123]) that provides several wavelength references, but there were no recordings made at the same occasion that checked the high energy situation again right after running several measurements at the lower ion beam energy. Hence, this spectrum carries the same overall uncertainty of about 0.02 nm (half a line width) as many of the delayed spectra discussed above. Further line identifications are required to ascertain the anchor line identities and to determine the accuracy and precision of the wavelength scale.

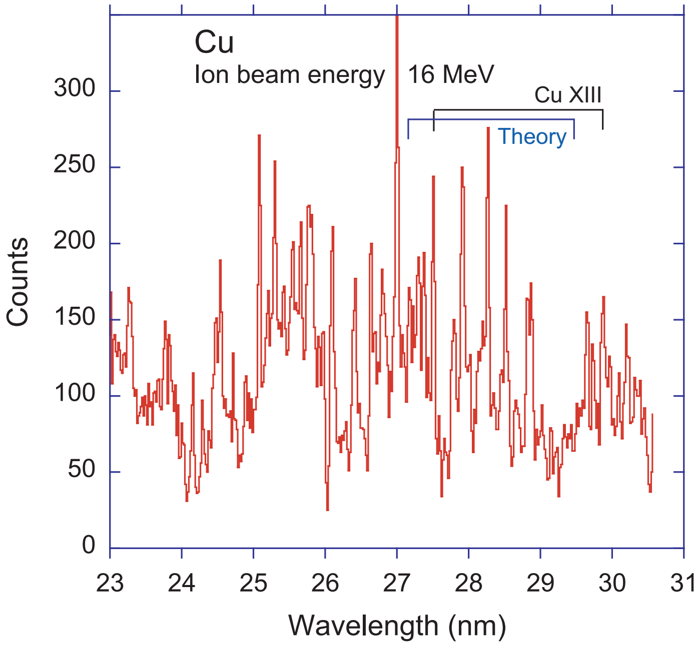

Figure 22. Beam–foil spectrum of Cu at an ion beam energy of 16 MeV. Line width (FWHM) 0.045 nm, observation near the foil. The charge state distribution maximum is near $q = 12+$, and ion charge states $q = 9+$ to $q = 15+$ are expected to contribute. The marked Cu XIII line pair is discussed in the text. Black marker: experiment [50], blue marker: theory [43].

With the contents of the NIST ASD database so slim for the charge states that are produced at an ion beam energy of 16 MeV, one might look for theory to indicate promising lines that are to be identified. For example (see Table 1), in Si-like Ni, the $3s^2 3p^2\ ^3P_2$–$3s^2 3p3d\ ^3F^o_3$ transition wavelength has been computed by two groups practically identically and within the 100 ppm uncertainty of the experimental value (see discussion above and [38,39]). For the same system in Fe, one of the computations [38] comes similarly close to the solar corona wavelength measurement, while the other differs by about 400 ppm. For the same system in Cu, the same computations agree with each other within 100 ppm, but the experimental error measure is an order of magnitude larger, and the only available beam-foil measurement of this line does not yield a reference that is suitable for a determination of the computational accuracy. This inconsistency along the isoelectronic sequence issues a warning about the need for testing and further refinement for all such computations. They may represent the best ability and knowledge, but without intrinsic tests of accuracy, their quality remains uncertain. The example just mentioned is of an ion with four electrons in the valence shell (two of them in the open sub-shell); below is an example of an ion with more electrons in the same shell, and it shows that each atomic system poses different challenges.

This being said, the computations are most helpful for spectral modeling and for some details and certain trends. For example, in delayed spectra of Cu, there are groups of weak lines in the vicinity of the intercombination lines of Mg- through Si-like ions. Theory [123] suggests that these belong to intercombination decays of sextet levels in P-like ions. Decays of three 3d $J = 7/2$ levels in such P-like ions have been discussed in [60], and the corresponding levels in S-like ions have been discussed in [124]. These levels are long lived because they differ by more than two units in total angular momentum from the $J = 3/2$ ground state, and thus they cannot decay there by an electric dipole transition. As a result, there are quite a number of excited levels with millisecond lifetimes. This has been corroborated by the recent computations by Wang et al. [40].

With such long lifetimes, the signal expected in the beam–foil observation geometry is too weak to be notable, by several orders of magnitude. Such long-lived decays have, however, been seen as cascades in experiments at a heavy-ion storage ring (see, for example, [125–129]). Amusingly, the presence of such slow cascades has been proven by these decay curve measurements that involved a very limited spectral resolution, but there is no practical method available yet to perform direct spectroscopy on such long-lived excited levels. The long lifetimes call for time-integrated observations at a very low particle density, such as in an EBIT; however, the excitation efficiency of such levels that are not easily populated directly from the ground state is very low there. The same problem pertains, of course, to many atomic systems with an open $n = 3$ valence shell.

The spectrum of Figure 22 is only indirectly related to the measurement problems in the delayed spectra, that is, by the need to find wavelength references. This spectrum has been recorded close to the exciter foil, and, consequently, it should be dominated by the emission of moderately short-lived levels, of Cu ions around charge state $q = 12+$. Level populations usually are the highest for the ground state, and lower for more energetic levels. Consequently, in a Cl-like atomic system, one should expect the decays of the lowest (displaced) term, the $3s3p^6\ ^2S_{1/2}$ level, to the two $3s^23p^5\ ^2P^o_{3/2,1/2}$ levels of the ground term, to give rise to prominent lines. According to the computations by Wang et al. [43], these lines have wavelengths of 27.175 nm and 29.465 nm, respectively. The calculated upper level lifetime is 148 ps; the wavenumber difference of the two lines is given by the (experimentally known from isoelectronic systems) fine structure interval of the $3s^23p^5\ ^2P^o$ ground term. Transitions of this type have been seen in many beam–foil spectra.

Let us start a first attempt at line identification in Figure 22 from the predicted wavelengths. There is no particularly bright line in the spectrum, nor is there a prominent candidate line pair right at the computed wavelengths, but several possible candidates lie in the vicinity. If a line near 27.175 nm was the right line to start with, a candidate of peak signal 150 counts, the second line should show a peak signal of about 60 counts (weaker than the first by the predicted line ratio of 1:2.4), which would make it part of an unresolved line group. If instead the brightest line of the spectrum, near 27.0 nm, with a peak signal of 350 counts, was associated with the stronger line of the doublet mentioned, the other line should appear near 29.3 nm, where no suitable second line is seen. There are several more options. Guided by older experimental work on many other elements, the lines of present interest have been found in beam–foil spectra of Cu, too, at wavelengths of 27.480 nm and 29.814 nm, respectively [50], 1% away from the predictions by Wang et al. [43]. Evidently, the two experimental wavelengths for the most fundamental transition array (between the ground term and the first excited term) in Cu XIII differ somewhat from even very good recent computations. 1% may seem a small error, but, in the case of Si-like Fe spectra, we have discussed agreement of experiment and theory at the 100 ppm level, which is two orders of magnitude better than this 10,000 ppm error achieved by a similar computational approach for a Cl-like Cu ion. Moreover, beam–foil lifetime measurements [50] point to a value in the middle of the factor-of-two scatter range of the various predictions of transition rates.

In the S-like spectrum Cu XIV, a number of intercombination decays of $3s^23p^33d\ ^5D^o_J$ levels to the $3s^23p^4$ ground configuration fall into or close to the wavelength range of the spectrum in Figure 22, but the predicted lines are not recognizable here. This is not a shortcoming of theory, but is due to a property of the beam–foil light source. Most of the upper levels have theoretical lifetimes (see, for example, [41]) in the range of a few nanoseconds. Such decays are best seen away from the exciter foil [123] because close to the foil the multitude of decays of short-lived levels dominates. Any attempt at spectrum analysis has to take the observational setting and conditions into account. These conditions strongly influence which transitions are likely to be seen.

3. Discussion

The availability of a reasonably well calibrated and resolved spectrum as shown in Figure 22 in combination with atomic structure computations that use up-to-date implementations of atomic structure theory does not immediately yield line identification. It is obvious that atomic structure computations have not yet reached their goal of high accuracy in all atomic systems. How accurate some of the most recent computations of such systems are (see the above citations and, for example, [41–43]) can only be established by successful line identifications. One path to get there would be spectrum simulations based on collisional-radiative modeling, which might enable visual pattern recognition of line intensities and spacings. Predictions on line intensities, however, relate to transition probabilities (a serious challenge to theory) and collision cross sections (another difficult field). Without reliable level populations and transition rates, the computations at least indicate which transitions to expect (in the present context, preferably unbranched decays of levels with lifetimes in the range from 0.1 ns to about 20 ns) among the many more that are possible in principle.

Thus far, the accuracy of atomic structure computations is often judged by comparison to the computational results of others (not a reliable measure!) or by comparison to experimental data. In multi-electron systems, this usually means the best (not necessarily good) agreement with some of the low-lying levels (but not necessarily with displaced terms) and an increasing mismatch with higher-lying levels. It would be good if intrinsic measures permitted estimates of whether advanced computations were likely to achieve errors as small as 100 ppm (on certain levels of interest) instead of the presently more typical 1%. It is similarly obvious that more and better spectroscopic data would be advantageous; experimental data in the 100 ppm quality class are not too common either.

A systematic beam–foil spectroscopic approach towards completion of the knowledge on EUV spectra of iron group elements would require wide spectral ranges to be recorded at many ion beam energies, at various delays after excitation, and at high spectral resolution. This would be very time-consuming in terms of accelerator operating time, and thus demanding in manpower and research funds. Multichannel detectors are costly to obtain, but would help to reduce the operation costs. Spectroscopy has rarely enjoyed sufficient funding for such a systematic approach; it is much more common to systematize and interconnect information from spotlight observations. Atomic structure computations have a high potential and carry many hopes for facilitating atomic spectrum analysis; they have made significant progress, but the goal of disentangling by ab initio techniques such spectra as the ones shown here is not yet in reach. The complexity and richness of the beam–foil spectra of many-electron systems defies the present toolbox of computational spectrum analysis. For key elements of spectrum analysis, systematic trends of fine structure intervals, and the like, we still rely on the half century of experimental and analytical work by Bengt Edlén.

Funding: This research received no external funding.

Data Availability Statement: Data files are available from the author on request.

Acknowledgments: Part of this work was performed under the auspices of the US Department of Energy by Lawrence Livermore National Laboratory under Contract DE-AC52-07NA27344 and profited from support by NASA's HTIDeS (Heliophysics Technology and Instrument Development for Science) contract NNH16AC82I.

Conflicts of Interest: The author declares no conflict of interest.

References

1. Edlén, B. Die Deutung der Emissionslinien im Spektrum der Sonnenkorona. *Zeits. Astrophys.* **1943**, *22*, 30–64.
2. Grotrian, W. Zur Frage der Deutung der Linien im Spektrum der Sonnenkorona. *Naturwissenschaften* **1939**, *27*, 214. [CrossRef]
3. Fawcett, B.C.; Gabriel, A.H.; Griffin, W.G.; Jones, B.B.; Wilson, R. Observations of the Zeta spectrum in the wave-length range 16 Å–400 Å. *Nature* **1963**, *200*, 1303–1304. [CrossRef]
4. Fawcett, B.C.; Gabriel, A.H. New spectra of the iron transition elements of astrophysical interest. *Astrophys. J.* **1965**, *141*, 343–355. [CrossRef]
5. Gabriel, A.H.; Fawcett, B.C.; Jordan, C. Classification of iron lines in the spectrum of the Sun and Zeta in the range 167 Å to 220 Å. *Nature* **1965**, *206*, 390–392. [CrossRef]
6. Kelly, R.L.; Palumbo, L.J. *Atomic and Ionic Emission Lines Below 2000 Å, Hydrogen through Krypton*; NRL: Washington, DC, USA, 1978.
7. Kelly, R.L. Atomic and ionic spectrum lines below 2000 Angstroms: Hydrogen through krypton. *J. Phys. Chem. Ref. Data* **1987**, *16* (Suppl. 1), 1–659.
8. Fawcett, B.C. Wavelengths and classifications of emission lines due to $2s^22p^n$-$2s2p^{n+1}$ and $2s2p^n$-$2p^{n+1}$ transitions, $Z \leq 28$. *At. Data Nucl. Data Tab.* **1975**, *16*, 135–164. [CrossRef]
9. Kramida, A. Cowan code: 50 years of growing impact on atomic physics. *Atoms* **2019**, *7*, 64. [CrossRef]
10. Ralchenko, Y.; Kramida, A. Development of NIST atomic data bases and online tools. *Atoms* **2020**, *8*, 56. [CrossRef]
11. Kramida, A.; Ralchenko, Yu.; Reader, J.; NIST ASD Team. *NIST Atomic Spectra Database*, Version 5.7.1; National Institute of Standards and Technology: Gaithersburg, MD, USA, 2019. Available online: https://physics.nist.gov/asd (accessed on 1 June 2021).
12. Shirai, T.; Funatake, Y.; Mori, K.; Sugar, J.; Wiese, W.L.; Nakai, Y. Spectral data and Grotrian diagrams for highly ionized iron, Fe VIII-XXVI. *J. Phys. Chem. Ref. Data* **1990**, *19*, 127–275. [CrossRef]
13. Dere, K.P.; Landi, E.; Mason, H.E.; Monsignori Fossi, B.C.; Young, P.R. CHIANTI—An atomic database for emission lines. *Astrophys. J.* **1997**, *125*, 149–173. [CrossRef]
14. Dere, K.P.; Landi, E.; Young, P.R.; Del Zanna, G.; Landini, M.; Mason, H.E. CHIANTI—An atomic database for emission lines. *Astron. Astrophys.* **2009**, *498*, 915–929. [CrossRef]
15. Landi, E.; Del Zanna, G.; Young, P.R.; Dere, K.P.; Mason, H.E. CHIANTI—An atomic database for emission lines. XII. Version 7 of the database. *Astrophys. J.* **2012**, *744*, 99. [CrossRef]
16. Landi, E.; Young, P.R.; Dere, K.P.; Del Zanna, G.; Mason, H.E. CHIANTI—An atomic database for emission lines. XII. Version 7 of the database. atomic database for emission lines. XIII. Soft X-ray improvements and other changes. *Astrophys. J.* **2013**, *763*, 86. [CrossRef]
17. Del Zanna, G.; Dere, K.P.; Young, P.R.; Landi, E.; Mason, H.E. CHIANTI—An atomic database for emission lines. Version 8. *Astron. Astrophys.* **2015**, *582*, 56 [CrossRef]
18. Del Zanna, G.; Young, P.R. Atomic data for plasma spectroscopy: The CHIANTI database, improvements and challenges. *Atoms* **2020**, *8*, 46. [CrossRef]
19. Brosius, J.W.; Thomas, R.J.; Davila, J.M.; Landi, E. Analysis of a solar active region extreme-ultraviolet spectrum from SERTS-97. *Astrophys. J.* **2000**, *543*, 1016–1026. [CrossRef]
20. Thomas, R.J.; Davila, J.M. EUNIS: A solar EUV normal-incidence spectrometer. *Proc. SPIE* **2001**, *4498*, 161–172.
21. Culhane, J.L.; Harra, L.K.; James, A.M.; Al-Janabi, K.; Bradley, L.J.; Chaudry, R.A.; Rees, K.; Tandy, J.A.; Thomas, P.; Whillock, M.C.R.; et al. The EUV Imaging Spectrometer for Hinode. *Solar Phys.* **2007**, *243*, 19–61. [CrossRef]
22. Pesnell, W.D.; Chamberlin, P.C.; Thompson, B.J. The $Solar Dynamics Observatory$ (SDO). *Sol. Phys.* **2012**, *275*, 3–15. [CrossRef]
23. Beiersdorfer, P.; Lepson, J.K.; Desai, P.; Díaz, F.; Ishikawa, Y. New identifications of Fe IX, Fe X, Fe XI, Fe XII, and Fe XIII lines in the spectrum of Procyon observd with the $Chandra X-ray Observatory$. *Astrophys. J. Suppl. Ser.* **2014**, *210*, 16. [CrossRef]
24. Träbert, E.; Beiersdorfer, P.; Brickhouse, N.S.; Golub, L. High-resolution laboratory spectra on the λ131 channel of the AIA instrument on board the $Solar Dynamics Observatory$. *Astrophys. J. Suppl. Ser.* **2014**, *211*, 14. [CrossRef]
25. Beiersdorfer, P.; Träbert, E. High-resolution laboratory measurements of coronal lines near the Fe IX line at 171 Å. *Astrophys. J.* **2018**, *854*, 114. [CrossRef]

26. Träbert, E.; Beiersdorfer, P.; Brickhouse, N.S.; Golub, L. High-resolution laboratory spectra of the λ193 channel of the atmospheric imaging assembly instrument on board *SolarDynamicsObservatory*. *Astrophys. J. Suppl. Ser.* **2014**, *215*, 6. [CrossRef]
27. Beiersdorfer, P.; Träbert, E.; Lepson, J.K.; Brickhouse, N.S.; Golub, L. High-resolution laboratory measurements of coronal lines in the 198–218 Å region. *Astrophys. J.* **2014**, *788*, 25. [CrossRef]
28. Träbert, E.; Beiersdorfer, P.; Brickhouse, N.S.; Golub, L. Low-density laboratory spectra near the He II λ304 line. *Astron. Astrophys.* **2016**, *586*, A115. [CrossRef]
29. Träbert, E.; Beiersdorfer, P. Low-density laboratory spectra near the λ335 channel of the SDO/AIA instrument. *Astron. Astrophys.* **2018**, *617*, A8. [CrossRef]
30. Träbert, E. Calcium and potassium spectra in the EUV. *Atoms* **2020**, *8*, 73. [CrossRef]
31. Träbert, E. EUV Beam-Foil Spectra of Scandium, Vanadium, Chromium, Manganese, Cobalt, and Zinc. *Atoms* **2021**, *9*, 23. [CrossRef]
32. Jönsson, P.; Alkauskas, A.; Gaigalas, G. Energies and E1, M1, E2 transition rates for states of the $2s^22p^5$ and $2s2p^6$ configurations in fluorine-like ions between Si VI and W LXVI. *At. Data Nucl. Data Tab.* **2013**, *99*, 431–446. [CrossRef]
33. Aggarwal, K.M. Radiative rates for E1, E2, M1, and M2 transitions in F-like ions with $12 \leq Z \leq 23$. *At. Data Nucl. Data Tab.* **2019**, *127–128*, 22–130. [CrossRef]
34. Jönsson, P.; Bengtsson, P.; Ekman, J.; Gustafsson, S.; Karlsson, L.B.; Gaigalas, G.; Froese Fischer, C.; Kato, D.; Murakami, I.; Sakaue, H.A.; et al. Relativistic CI calculations of spectroscopic data for the $2p^6$ and $2p^53l$ configurations in Ne-like ions between Mg III and Kr XXVII. *At. Data Nucl. Data Tab.* **2012**, *100*, 1–154. [CrossRef]
35. Kim, Y.-K.; Baik, D.H.; Indelicato, P.; Desclaux, J.P. Resonance transition energies of Li-, Na-, and Cu-like ions. *Phys. Rev. A* **1991**, *44*, 148–166. [CrossRef] [PubMed]
36. Santana, J.A. Relativistic MR-MP energy levels: Low-lying states in the Mg isoelectronic sequence. *At. Data Nucl. Data Tab.* **2016**, *111–112*, 87–186. [CrossRef]
37. Vilkas, M.J.; Ishikawa, Y. Relativistic multireference many-body perturbation theory calculations for siliconlike argon, iron and krypton ions. *J. Phys. B At. Mol. Opt. Phys.* **2003**, *36*, 4641–4650. [CrossRef]
38. Vilkas, M.J.; Ishikawa, Y. High-accuracy calculations of term energies and lifetimes of silicon-like ions with nuclear charges Z = 24–30. *J. Phys. B At. Mol. Opt. Phys.* **2004**, *37*, 1803–1816. [CrossRef]
39. Jönsson, P.; Radžiūtė, L.; Gaigalas, G.; Godefroid, M.; Marques, J.P.; Brage, T.; Froese Fischer, C.; Grant, I. Accurate multiconfiguration calculations of energy levels, lifetimes, and transition rates for the silicon isoelectronic sequence Ti IX–Ge XIX, Sr XXV, Zr XXVII, Mo XXIX. *Astron. Astrophys.* **2016**, *585*, A26. [CrossRef]
40. Wang, K.; Jönsson, P.; Gaigalas, G.; Radžiūtė, L.; Rynkun, P.; Del Zanna, G.; Chen, C.Y. Energy levels, lifetimes, and transition rates for P-like ions from Cr X to Zn XVI from large-scale relativistic multiconfiguration calculations. *Astrophys. J. Suppl. Ser.* **2018**, *235*, 27. [CrossRef]
41. Wang, K.; Song, C.X.; Jönsson, P.; Del Zanna, G.; Schiffmann, S.; Godefroid, M.; Gaigalas, G.; Zhao, X.H.; Si, R.; Chen, C.Y.; et al. Benchmarking atomic data from large-scale multiconfiguration Dirac-Hartree-Fock calculations for astrophysics: S-like Ions from Cr IX to Cu XIV. *Astrophys. J. Suppl. Ser.* **2018**, *239*, 30. [CrossRef]
42. Aggarwal, K.M. Energy levels and radiative rates for transitions in S-like Sc VI, V VIII, Cr IX, and Mn X. *At. Data Nucl. Data Tab.* **2020**, *131*, 101284. [CrossRef]
43. Wang, K.; Jönsson, P.; Del Zanna, G.; Godefroid, M.; Chen, Z.B.; Chen, C.Y.; Yan, J. Large-scale multiconfiguration Dirac-Hartree-Fock calculations for astrophysics: Cl-like Ions from Cr VIII to Zn XIV. *Astrophys. J. Suppl. Ser.* **2020**, *246*, 1. [CrossRef]
44. Jönsson, P.; Gaigalas, G.; Rynkun, P.; Radžiūtė, L.; Ekman, J.; Gustafsson, S.; Hartman, H.; Wang, K.; Godefroid, M.; Froese Fischer, C.; et al. Multiconfiguration Dirac-Hartree-Fock Calculations with Spectroscopic Accuracy: Applications to Astrophysics. *Atoms* **2017**, *5*, 16. [CrossRef]
45. Hutton, R.; Engström, L.; Träbert, E. Observation of a discrepancy between experimentally determined atomic lifetimes and relativistic predictions for highly ionized members of the Na I isoelectronic sequence. *Phys. Rev. Lett.* **1988**, *60*, 2469–2472. [CrossRef] [PubMed]
46. Jupén, C.; Engström, L.; Hutton, R.; Träbert, E. Identification of the core-excited $2p^53s3p\ ^4D_{7/2}$–$2p^53s3d\ ^4F_{9/2}$ transition in Na-like ions ranging from S VI to Cu XIX. *J. Phys. B At. Mol. Opt. Phys.* **1988**, *21*, L347–L351. [CrossRef]
47. Jupén, C.; Engström, L.; Hutton, R.; Reistad, N.; Westerlind, M. Analysis of core-excited n = 3 configurations in S VI, Cl VII, Ar VIII and Ti XII. *Phys. Scr.* **1990**, *42*, 44–50. [CrossRef]
48. Thornbury, J.F.; Träbert, E.; Möller, G.; Heckmenn, P.H. Beam–foil lifetime measurements on the $3s^24s\ ^2S$ states in the aluminium sequence, Cl V to Mn XIII. *Phys. Scr.* **1990**, *42*, 700–704. [CrossRef]
49. Engström, L.; Kirm, M.; Bengtsson, P.; Maniak, S.T.; Curtis, L.J.; Träbert, E.; Doerfert, J.; Granzow, J. Extended analysis of intensity anomalies in the Al I isoelectronic sequence. *Phys. Scr.* **1995**, *52*, 516–521. [CrossRef]
50. Träbert, E. Experimental checks on calculations for Cl-, S- and P-like ions of the iron group elements. *J. Phys. B At. Mol. Opt. Phys.* **1996**, *29*, L217–L224. [CrossRef]
51. Träbert, E. The allure of high total angular momentum levels in multiply-excited ions. *Atoms* **2019**, *7*, 103. [CrossRef]
52. Jupén, C.; Träbert, E. The $2p^43s$, 3p and 3d configurations in K XI. *J. Phys. B At. Mol. Opt. Phys.* **2001**, *34*, 3053–3061. [CrossRef]
53. Jupén, C.; Träbert, E.; Doerfert, J.; Granzow, J.; Jaensch, R. Analysis of 3s, 3p, 3d and 4f Configurations of Sc XIII and V XV. *Phys. Scr.* **2002**, *66*, 150–158. [CrossRef]

54. Ishikawa, Y.; López-Encarnación, J.M.; Träbert, E. $N = 3 - 3$ transitions of Ne-like ions in the iron group, especially Ca^{10+} and Ti^{12+}. *Phys. Scr.* **2009**, *79*, 025301. [CrossRef]
55. Träbert, E.; Reistad, N.; Hutton, R. Intercombination decay of 3s3p $^3P^o_1$ in Mg I-like Ni and Cu. *Z. Phys. D* **1986**, *1*, 331–332. [CrossRef]
56. Träbert, E. Wavelength and lifetime data on intercombination transitions in the Si I isoelectronic sequence. *Z. Phys. D* **1986**, *2*, 213–222. [CrossRef]
57. Träbert, E.; Hutton, R.; Martinson, I. Identification of intercombination transitions in Fe XIV and Fe XIII in the spectra of foil-excited ions and solar flares. *Mon. Not. R. Astron. Soc.* **1987**, *227*, 27P–31P. [CrossRef]
58. Träbert, E.; Hutton, R.; Martinson, I. Intercombination lines in delayed beam–foil spectra. *J. Opt. Soc. Am. B* **1988**, *5*, 2173–2182. [CrossRef]
59. Träbert, E.; Brandt, M.; Doerfert, J.; Granzow, J.; Heckmann, P.H.; Meurisch, J.; Martinson, I.; Hutton, R.; Myrnäs, R. Beam–foil measurements on intercombination transitions in Cl-like ions of elements Mn through Zn. *Phys. Scr.* **1993**, *48*, 580–585. [CrossRef]
60. Träbert, E. Solar EUV line identifications from delayed beam–foil spectra. *Mon. Not. R. Astron. Soc.* **1998**, *297*, 399–404. [CrossRef]
61. Träbert, E. Radiative-lifetime measurements on highly-charged ions. In *Accelerator-Based Atomic Physics Techniques and Applications*; Shafroth, S.M., Austin, J.C., Eds.; American Institute of Physics: Washington, DC, USA, 1997; pp. 567–607.
62. Träbert, E. Beam–foil spectroscopy—Quo vadis? *Phys. Scr.* **2008**, *78*, 038103. [CrossRef]
63. Middleton, R. *A Negative-Ion Cookbook*; Department of Physics, University of Pennsylvania: Philadelphia, PA, USA, 1990.
64. Brand, K. Performance of the reflected beam sputter source. *Rev. Phys. Appl.* **1977**, *12*, 1453–1457. [CrossRef]
65. Sayer, R.O. Semi-empirical formulas for heavy-ion stripping data. *Rev. Phys. Appl.* **1977**, *12*, 1543–1546. [CrossRef]
66. Delaunay, B. Heavy-ion stripping. *Nucl. Instrum. Meth.* **1977**, *146*, 101–113. [CrossRef]
67. Shima, K.; Kuno, N.; Yamanouchi, M.; Tawara, H. Equilibrium charge fractions of ions of $Z = 4 - 92$ emerging from a carbon foil. *At. Data Nucl. Data Tab.* **1992**, *51*, 173–241. [CrossRef]
68. Johnson, B.M.; Jones, K.W.; Gregory, D.C.; Kruse, T.H.; Träbert, E. Beam–foil lifetimes of $n = 3$ levels in Fe XIII to Fe XVI. I. Experiment using position sensitive detection. *Phys. Lett.* **1981**, *86A*, 285–288. [CrossRef]
69. Träbert, E.; Jones, K.W.; Johnson, B.M.; Gregory, D.C.; Kruse, T.H. Beam–foil lifetimes of $n = 3$ levels in Fe XIII to Fe XVI. II. Analysis of decay curves. *Phys. Lett.* **1982**, *87A*, 336–340. [CrossRef]
70. Armour, I.A.; Myers, E.G.; Silver, J.D.; Träbert, E. Improved wavelengths for the 1s2s $^3S_1$–1s2p $^3P_{0,2}$ transitions in helium-like Si^{12+}. *Phys. Lett.* **1979**, *75A*, 45–46. [CrossRef]
71. Bashkin, S.; Träbert, E.; Heckmann, P.H.; Buttlar, H.V.; Brand, K. Beam–foil study of titanium in the EUV using foils of different materials. *Phys. Scr.* **1983**, *28*, 193–200. [CrossRef]
72. Santana, J.A.; Träbert, E. Resonance and intercombination lines in Mg-like ions of atomic numbers Z = 13–92. *Phys. Rev. A* **2015**, *91*, 022503. [CrossRef]
73. Aggarwal, K.M.; Keenan, F.P. Energy levels and radiative rates for transitions in Ti X. *Phys. Scr.* **2013**, *88*, 025303. [CrossRef]
74. Pinnington, E.H.; Ansbacher, W.; Träbert, E.; Heckmann, P.H.; Hellmann, H.M.; Möller, G. Beam–foil lifetime study of the $n = 3$ complex in Al-like Ti^{9+}. *Z. Phys. D At. Mol. Clust.* **1987**, *6*, 241–247. [CrossRef]
75. Pinnington, E.H.; Ansbacher, W.; Tauheed, A.; Träbert, E.; Heckmann, P.H.; Möller, G.; Blanke, J.H. Beam–foil lifetime study of Al-like titanium, iron and nickel. *Z. Phys. D At. Mol. Clust.* **1997**, *17*, 5–9. [CrossRef]
76. Träbert, E. Identification of $n = 3$, $\Delta n = 0$ transitions of Ne I-like Ti XIII in the beam–foil spectrum of titanium. *Z. Phys. A At. Nucl.* **1984**, *319*, 25–32. [CrossRef]
77. Träbert, E. The $n = 3$ level structure of neonlike Ti^{12+}. *Nucl. Instrum. Meth. Phys. Res. B* **1985**, *9*, 626–629. [CrossRef]
78. Träbert, E. Beam–foil lifetime study of neon-like Ti^{12+}. *Z. Phys. D At. Mol. Clust.* **1986**, *1*, 283–286. [CrossRef]
79. Jupén, C.; Litzén, U.; Kaufman, V.; Sugar, J. Ne-like Ca XI–Mn XVI $2p^53\ell$–$2p^54\ell$ transition arrays and energy levels. *Phys. Rev. A* **1987**, *35*, 116–130. [CrossRef] [PubMed]
80. Jupén, C.; Reistad, N.; Träbert, E.; Blanke, J.H.; Heckmann, P.H.; Hellmann, H.M.; Hucke, R. The $2p^43s$, 3p and 3d configurations of thirteen times ionized titanium, Ti XIV. *Phys. Scr.* **1985**, *32*, 527–533. [CrossRef]
81. Träbert, E.; Jupén, C. Identification of $2s^22p^53p$ $^1S_0$ decays in the spectra of neon-like ions. *Phys. Scr.* **1987**, *36*, 586–590. [CrossRef]
82. Jupén, C.; Litzén, U.; Träbert, E. Observation of transitions from inner-shell $2s2p^63\ell$ states in neon-like ions. *Phys. Lett. A* **1996**, *214*, 273–278. [CrossRef]
83. Jupén, C.; Litzén, U.; Träbert, E. The Spectrum and Term System of Neonlike Titanium, Ti Xlll. *Phys. Scr.* **1996**, *53*, 139–148. [CrossRef]
84. Träbert, E.; Heckmann, P.H.; Raith, B.; Sander, U. Beam–foil based efficiency calibration of a grazing-incidence spectrometer. *Phys. Scr.* **1980**, *22*, 363–366. [CrossRef]
85. Träbert, E. Extended relative efficiency calibration of a grazing incidence monochromator and applications in fast-beam spectroscopy. *Phys. Scr.* **1984**, *T 8*, 112–116. [CrossRef]
86. Curtis, L.J.; Martinson, I. Lifetimes of excited states in highly charged ions. In *Atomic Physics with Heavy Ions*; Springer Series on Atoms and Plasmas; Beyer, H.F., Shevelko, V.P., Eds.; Springer: Berlin/Heidelberg, Germany, 1999; Volume 26, pp. 197–218. [CrossRef]
87. Träbert, E. Intercombination transitions: LIfetime measurements by beam–foil spectroscopy and other techniques confronted with theoretical trends. *Phys. Scr.* **1993**, *48*, 699–713. [CrossRef]

88. Del Zanna, G. Benchmarking atomic data for astrophysics: Fe VII and other cool lines observed by Hinode EIS. *Astron. Astrophys.* **2009**, *508*, 501–511. [CrossRef]
89. Del Zanna, G. Benchmarking atomic data for astrophysics: Fe VIII EUV lines. *Astron. Astrophys.* **2009**, *508*, 513–524. [CrossRef]
90. Del Zanna, G.; Storey, P.J.; Badnell, N.R.; Mason, H.E. Atomic data for astrophysics: Fe IX. *Astron. Astrophys.* **2014**, *565*, A77. [CrossRef]
91. Del Zanna, G.; Berrington, K.A.; Mason, H.E. Benchmarking atomic data for astrophysics: Fe X EUV lines. *Astron. Astrophys.* **2004**, *422*, 731–749. [CrossRef]
92. Del Zanna, G. Benchmarking atomic data for astrophysics: Fe XI. *Astron. Astrophys.* **2010**, *514*, A41. [CrossRef]
93. Del Zanna, G.; Mason, H.E. Benchmarking atomic data for astrophysics: Fe XII. *Astron. Astrophys.* **2005**, *433*, 731–744. [CrossRef]
94. Del Zanna, G.; Storey, P.J.; Badnell, N.R.; Mason, H.E. Atomic data for astrophysics: Fe XII soft X-ray lines. *Astron. Astrophys.* **2012**, *543*, A139. [CrossRef]
95. Del Zanna, G. Benchmarking atomic data for astrophysics: Fe XIII EUV lines. *Astron. Astrophys.* **2011**, *533*, A12. [CrossRef]
96. Träbert, E.; Ishikawa, Y.; Santana, J.A.; Del Zanna, G. The $3s^23p3d\ ^3F^o$ term in the Si-like spectrum of Fe (Fe XIII). *Can. J. Phys.* **2011**, *89*, 403–412. [CrossRef]
97. Del Zanna, G.; Ishikawa, Y. Benchmarking atomic data for astrophysics: Fe XVII EUV lines. *Astron. Astrophys.* **2009**, *508*, 1517–1526. [CrossRef]
98. Del Zanna, G. Benchmarking atomic data for astrophysics: Fe XVII X-ray lines. *Astron. Astrophys.* **2011**, *536*, A59. [CrossRef]
99. Del Zanna, G. Benchmarking atomic data for astrophysics: A first look at the soft X-ray lines. *Astron. Astrophys.* **2012**, *546*, A97. [CrossRef]
100. Del Zanna, G. Benchmarking atomic data for the CHIANTI atomic database: Coronal lines observed by Hinode EIS. *Astron. Astrophys.* **2012**, *537*, A38. [CrossRef]
101. Beiersdorfer, P. A “brief" history of spectroscopy on EBIT. *Can. J. Phys.* **2008**, *86*, 1–10. [CrossRef]
102. Liang, G.Y.; Baumann, T.M.; Crespo López-Urrutia, J.R.; Epp, S.W.; Tawara, H.; Conchar, A.; Mokler, P.H.; Zhao, G.; Ullrich, J. Extreme-ultraviolet spectroscopy of Fe VI–Fe XV and its diagnostic application for electron beam ion trap plasmas. *Astrophys. J.* **2009**, *696*, 2275–2289. [CrossRef]
103. Träbert, E.; Beiersdorfer, P.; Pinnington, E.H.; Utter, S.B.; Vilkas, M.J.; Ishikawa, Y. Experiment and theory in interplay on high-Z few-electron ion spectra from foil-excited ion beams and electron beam ion traps. *J. Phys. Conf. Ser.* **2007**, *58*, 93–96. [CrossRef]
104. Träbert, E. Extreme ultraviolet spectra of highly charged Fe ions in the laboratory versus the excitation of spectra in astrophysical environments. *Can. J. Phys.* **2017**, *95*, 777–782. [CrossRef]
105. Buchet, J.P.; Buchet-Poulizac, M.C.; Denis, A.; Désesquelles, J.; Druetta, M. Measurement of radiative lifetimes of low-lying excited states in sodiumlike, fluorinelike, and oxygenlike iron. *Phys. Rev. A* **1980**, *22*, 2061–2068. [CrossRef]
106. Buchet, J.P.; Buchet-Poulizac, M.C.; Denis, A.; Désesquelles, J.; Druetta, M.; Grandin, J.P.; Huet, M.; Husson, X.; Lecler, D. Radiative lifetimes and oscillator strengths for 2s-2p transitions in He-, Li-, and Be-like iron. *Phys. Rev. A* **1984**, *30*, 309–315. [CrossRef]
107. Buchet, J.-P.; Buchet-Poulizac, M.-C.; Denis, A.; Désesquelles, J.; Druetta, M.; Martin, S.; Grandin, J.P.; Husson, X.; Lesteven, I. Beam–foil study of the $2s^22p^53\ell$ and $2s2p^63\ell$ configurations of Fe XVll. *Phys. Scr.* **1985**, *31*, 364–368. [CrossRef]
108. Hutton, R.; Engström, L.; Träbert, E. Experimental oscillator strengths for the resonance lines in Na- and Mg-like iron. *Nucl. Instrum. Meth. Phys. Res. B* **1988**, *31*, 294–299. [CrossRef]
109. Kohstall, C.; Fritzsche, S.; Fricke, B.; Sepp, W.D.; Träbert, E. Comment on the lifetimes of the $3s3p^6\ ^2S_{1/2}$ level for chlorine-like ions. *Phys. Scr. T* **1999**, *80*, 482–484. [CrossRef]
110. Lepson, J.K.; Beiersdorfer, P.; Clementson, J.; Gu, M.F.; Bitter, M.; Roquemore, L.; Kaita, R.; Cox, P.G.; Safronova, A.S. EUV spectroscopy on NSTX. *J. Phys. B At. Mol. Opt. Phys.* **2010**, *43*, 144018. [CrossRef]
111. Weller, M.E.; Beiersdorfer, P.; Soukhanovskii, V.A.; Magee, E.W.; Scotti, F. Three new extreme ultraviolet spectrometers on NSTX-U for impurity monitoring. *Rev. Sci. Instrum.* **2016**, *87*, 11E324. [CrossRef]
112. Beiersdorfer, P.; Magee, E.W.; Träbert, E.; Chen, H.; Lepson, J.K.; Gu, M.-F.; Schmidt, M. Flat-field grating spectrometer for high-resolution soft x-ray and extreme ultraviolet measurements on an electron beam ion trap. *Rev. Sci. Instrum.* **2004**, *75*, 3723–3726. [CrossRef]
113. Arthanayaka, T.; Beiersdorfer, P.; Brown, G.V.; Gu, M.F.; Hahn, M.; Hell, N.; Lockard, T.; Savin, D.W. Laboratory calibrations of Fe XII–XIV line-intensity ratios for electron density diagnostics. *Astrophys. J.* **2020**, *890*, 77. [CrossRef]
114. Froese Fischer, C. Towards accurate transition data for $3p^2$, $3p^3$, $3p^4$ levels of Fe, Co and Ni ions. *J. Phys. B At. Mol. Opt. Phys.* **2010**, *43*, 074020. [CrossRef]
115. Hutton, R.; Jupén, C.; Träbert, E.; Heckmann, P.H. Spectroscopy of highly ionised copper and nickel. *Nucl. Instrum. Meth. Phys. Res. B* **1987**, *23*, 297–299. [CrossRef]
116. Hutton, R.; Reistad, N.; Martinson, I.; Träbert, E.; Heckmann, P.H.; Blanke, J.H.; Hellmann, H.M.; Hucke, R. Lifetimes of some low-lying levels in Ni XVII. *Phys. Scr.* **1987**, *35*, 300–302. [CrossRef]
117. Träbert, E.; Reistad, N.; Martinson, I.; Hutton, R. Beam–foil lifetime data for $3s\ 3p^3$ and $3s^23p3d$ levels of Si-like Ni^{14+}. *Z. Phys. D At. Mol. Clust.* **1989**, *11*, 207–211. [CrossRef]
118. Pinnington, E.H.; Tauheed, A.; Träbert, E.; Blanke, J.H.; Heckmann, P.H.; Möller, G. Energy level assignments in Ni XVI. *Nucl. Instrum. Meth. Phys. Res. B* **1989**, *40/41*, 235–238. [CrossRef]

119. Träbert, E.; Jupén, C.; Fritzsche, S. EUV line identifications and lifetime measurements in highly-charged ions of the iron group. *Phys. Scr.* **1999**, *80*, 463–465. [CrossRef]
120. Biémont, E. Energy-level scheme and oscillator strengths for the 3s-3p and 3p-3d transitions in silicon sequence for elements vanadium through nickel. *Phys. Scr* **1986**, *33*, 324–335. [CrossRef]
121. Dere, K.P. Spectral lines observed in solar flares between 171 and 630 Angstroms. *Astrophys. J.* **1978**, *221*, 1062–1067. [CrossRef]
122. Del Zanna, G.; Storey, P.J.; Mason, H.E. Atomic data for astrophysics: Ni XV. *Astron. Astrophys.* **2014**, *567*, A18. [CrossRef]
123. Träbert, E.; Fritzsche, S.; Jupén, C. Sextet levels in the phosphorus-like ion Cu^{14+}. *Eur. Phys. J. D* **1998**, *3*, 13–20.
124. Fritzsche, S.; Dong, C.Z.; Träbert, E. Energy levels, lifetimes and branch fractions for Fe XI. *Mon. Not. R. astron. Soc.* **2000**, *318*, 263–272. [CrossRef]
125. Träbert, E.; Gwinner, G.; Wolf, A.; Knystautas, E.J.; Garnir, H.-P.; Tordoir, X. M1/E2 transition rates in Fe X through Fe XIII measured at a heavy-ion storage ring. *J. Phys. B At. Mol. Opt. Phys.* **2002**, *35*, 671–689. [CrossRef]
126. Träbert, E.; Calamai, A.G.; Gwinner, G.; Knystautas, E.J.; Pinnington, E.H.; Wolf, A. M1/E2/M2 decay rates in Fe VII, Fe IX, Fe X and Fe XIII measured using a heavy-ion storage ring. *J. Phys. B At. Mol. Opt. Phys.* **2003**, *36*, 1129–1141. [CrossRef]
127. Träbert, E.; Saathoff, G.; Wolf, A. Ground configuration level lifetimes in S-like Ni and Cu ions (Ni XIII and Cu XIV) measured at a heavy-ion storage ring. *Eur. Phys. J. D* **2004**, *30*, 297–302. [CrossRef]
128. Träbert, E.; Reinhardt, S.; Hoffmann, J.; Wolf, A. M1 transition rates in Co XI and Co XIII measured at a heavy-ion storage ring. *J. Phys. B At. Mol. Opt. Phys.* **2006**, *39*, 945–954. [CrossRef]
129. Träbert, E.; Hoffmann, J.; Krantz, C.; Wolf, A.; Ishikawa, Y.; Santana, J.A. Atomic lifetime measurements on forbidden transitions of Al-, Si-, P- and S-like ions at a heavy-ion storage ring. *J. Phys. B At. Mol. Opt. Phys.* **2009**, *42*, 025002. [CrossRef]